Design of a 50-Watt Air Supplied Turbogenerator

by

STEVAN JOVANOVIC

Diplôme d'Ingénieur, Ecole Centrale Paris, France (2007)

Submitted to the Department of Aeronautics and Astronautics

in Partial Fulfillment of the Requirements for the Degree of

Master of Science in Aeronautics and Astronautics

at the

MASSACHUSETTS INSTITUTE OF TECHNOLOGY

March 2008

[June 2008]

Signature of Author..

Department of Aeronautics and Astronautics

March 7, 2008

Certified by...

.....

Zoltán S. Spakovszky

H. N. Slater Associate Professor of Aeronautics and Astronautics
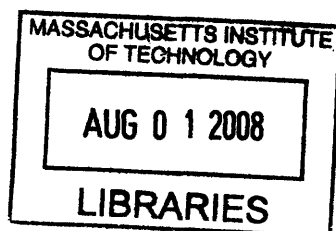
Thesis Supervisor

Accepted by......................................

Prof. David L. Darmofal

Associate Department Head

Chair, Committee on Graduate Students

Design of a 50 Watt Air Supplied Turbogenerator

by

STEVAN JOVANOVIC

Abstract

This thesis presents the design of a high-pressure-ratio, low-flow turbogenerator with 50 W electrical power output, designed to operate from a 5-bar air supply. The research shows that a MEMS-based silicon turbine in combination with a micro-machined generator can meet the design objectives of the turbogenerator.

The turbogenerator architecture comprises a single-stage radial inflow turbine and a direct coupled cylindrical permanent-magnet synchronous generator. To address its key design trade-offs and fundamental engineering challenges, the design space is first explored in terms of the key design variables: device diameter and rotor shaft speed. To guide the selection of the two variables, a simplified model for the scaling of turbine and generator power is developed. Next, the integrated turbine and generator design is analyzed and designed in detail. The minimum manufacturable turbine blade span is identified as the key challenge imposed by the low flow requirement. Furthermore, the small scale of the blades results in high rotational speeds. Since the turbine and generator are integrated, the high speed makes the generator design challenging because of manufacturing tolerances, material stress limitations and losses. Thus, the design trade-off is between generator complexity and turbine blade manufacturability. The analysis shows that the viable low-flow 50 W turbogenerator design space is narrowly constrained by the minimum blade span and the 5-bar pressure supply, demanding MEMS fabrication for the short turbine blades.

A single-stage MEMS radial turbine is designed in detail, and assessed for performance and manufacturability. The rotor speed at design conditions is 450,000 rpm with a rotor radius of 5 mm, a rotor blade span of 200 um, and a blade tip clearance of 20 um. Based on 3D RANS simulations, the turbine is predicted to achieve 48% total-to-static adiabatic efficiency and to produce 77 W of shaft power at a turbine mass flow of 1.45 g/s. Assuming a generator efficiency of 80% and a power electronics efficiency of 90% yields a net electrical turbogenerator power output of 50 W. End-wall losses are dominant in the planar turbine and a diffuser is included to reduce the pressure losses in the right exit turn. The final high-speed, low flow design integrates a MEMS turbine and a meso-scale permanent-magnet synchronous generator combined with hybrid ball bearings.

Thesis Supervisor: Zoltán S. Spakovszky
Title: H. N. Slater Associate Professor

Acknowledgements

First and foremost, I wish to thank my thesis advisor, Professor Spakovszky, and Professor Lang. I thank Professor Spakovszky for his invaluable guidance and support. This work would not have been possible without his talent and deep care for the project. With his very high expectations and standards, he kept the project, and more importantly me, on tract. Despite his intense schedule, he was willing to help and contribute an incredible amount of time when necessary, even until the very end, even despite a small dog, a broken foot, and a trip to the emergency room. He was an example for me and for everybody in the lab. I wish to express my sincere appreciation to him. The success of this project was also due to the help of Professor Lang and his professional as well as personal guidance. His knowledge, friendliness and enthusiasm made all the difference. He could always spare the time and listen to any of my concerns. It was most pleasant to work with him.

My time at MIT was an invaluable experience. I learned the meaning of quality research; it was certainly a challenging time, but with the help of my advisors I learned enormous amounts in terms of rigor and logic, and how to challenge your results (which I had to do rather often!). My experiences at MIT marked me and changed the way I will approach new problems – what more can one ask to learn in Graduate school? For all this, I am vey thankful.

I want to thank as well everybody in the GTL for their help, advice and good times. This includes Professor Epstein, who initially gave the opportunity to work on this project, Diana Park, who helped with some of the graphs, Holly Anderson, who helped with all the organizational issues, and all my labmates who made my experience in the GTL worthwhile: Sean, Isabelle, Andreas, Björn, and everybody else.

My journey at MIT would not have been possible without the love and support of my parents and brothers, and most importantly the unconditional love of Charity, who shared with me all the ups and downs.

Table of Contents

List of Figures

List of Tables

Nomenclature

Roman

c_p	specific heat at constant pressure
C	absolute flow velocity
h	blade span, specific enthalpy
L	length
$\dot{m}$	mass flow
M	Mach number
n	number of pole pairs, number of blades
R	radius
p	pressure
P	power
s	entropy
SF	safety factor
T	temperature, torque
U	rotor speed
w	specific work
W	relative flow velocity

Greek

α	flow angle in absolute reference frame
β	flow angle in relative reference frame
γ	specific heat ratio
Δ	finite change or difference
η	efficiency
ν	Poisson coefficient
ρ	density
π	pressure ratio
σ	shear stress, solidity, stage reaction
τ	temperature ratio
ϕ	flow coefficient
Ψ	work coefficient
Ω	shaft speed

Superscripts

ad	adiabatic

Subscripts

Exit	turbine exit
GE	generator

n	normal
PE	power electronics
s	static
t	total
T	turbine
tip	rotor tip

Acronyms

DRIE	Deep Reactive Ion Etching
SDM	Shape Deposition Manufacturing
MEMS	Micro Electro-Mechanical System

Chapter 1.   Introduction

1.1.   Motivation

This thesis investigates the design of a 50 W turbogenerator for which air is supplied at 5 bar. The major design goal is low mass-flow consumption for fixed turbogenerator power output, equivalent to high specific work and efficiency, since compressed air is considered a precious resource. Additional considerations are the simplicity of the design and the manufacturability of the components. The objectives of this thesis are to explore the design space and to define a viable turbogenerator architecture meeting the performance goals, manufacturing constraints, and tolerance requirements.

1.2.   Turbogenerators

1.2.1. Background and Concept

A possible replacement for electrical power supplies is to employ a turbogenerator that converts compressed air, available from a pressure line or tank, into electrical power. In this context, a turbogenerator, as illustrated in Figure 1-1, is used to convert the energy stored in the fluid into mechanical work, and to convert mechanical work into electrical work. There are several methods of extracting the energy stored in compressed air, but most commonly a turbine is used because of its simplicity and relatively higher power density. To transform mechanical work into electrical power, an electric generator can be used.
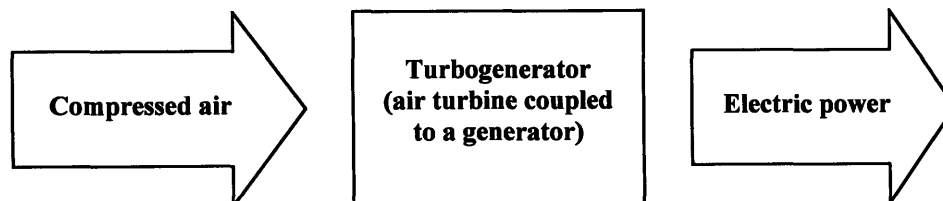
Figure 1-1: Schematic of Turbogenerator concept.

1.2.2. Review of 5 – 500 Watt Turbogenerators and Turbines

Turbogenerators with power outputs in the kilowatt range can be found for example in Auxiliary Power Units and Micro Gas Turbines. On a much smaller scale (10 mm or less in diameter) MEMS based turbines have been extensively investigated and developed to produce shaft power in the 10 W to 100 W range. A summary can be found in Jacobson and Epstein [15]. In order to achieve high power density, these devices need to operate at high rotational speeds (of order million rpm). This yields a major challenge for bearings and rotor dynamics and requires high-speed gas bearings. For a summary see Liu et al. [21]. An alternative approach to small scale turbomachinery is to use micro-machined components. The tables below summarize both MEMS-based micro-scale and meso-scale conventionally manufactured turbogenerator and turbine designs. A short summary of the relevant work is given next.

Table 1-1: Summary of 5-500 W single-stage radial turbines found in the literature

Reference	P_{shaft} (W)	$\dot{m}$ (g/s)	T_{t1} (K)	π (-)	Ω (rpm)	η_T (%)
MIT [26]	49[1]	0.29	1,600	2.1	1,200,000	54
Stanford [33]	72[2]	2.1	300	2.1	420,000	60
IHI [13]	344[1]	13.4	393	4	870,000	20

---

[1] Performance at design speed; no experimental data published to date

[2] Performance data estimated by author based on reported compressor performance[33]

Table 1-2: Summary of 5-500 W turbogenerator units found in the literature

Reference	P_{shaft} (W)	P_{el} (W)	$\dot{m}$ (g/s)	T_{t1} (K)	π (-)	Ω (rpm)	η_T (%)	Properties
MIT/GIT [1]	10	8	N/A	300	2.1	305,000	N/A	Off-the-shelf axial turbine coupled to MEMS generator
KUL [25]	28	16	2.9	300	1.8	100,000	18	Custom designed axial turbine coupled to commercial generator
ETH [20]	250	150	4.0	300	3.5	500,000	70	Custom designed generator coupled to off-the-shelf radial turbine

Three separate studies, at MIT, Stanford, and Tohoku University, focused on the design of single-stage radial turbines in the 50 W to 500 W range. As part of the Micro-Engine Project at MIT [26], a team developed a single-stage radial turbine with a 400 um blade span and a 6 mm diameter. At design conditions, this turbine produces 49 W of shaft power at a pressure ratio of 2.1. The challenge of fabricating the planar turbine with small features was addressed using deep reactive ion etching (DRIE), a fabrication method commonly used in computer chip manufacturing.

A team at Stanford University [33] designed and fabricated turbomachinery components for a miniature gas turbine engine. The single-stage radial turbine with a 12 mm diameter and a 250 um blade span was operated at 420,000 rpm. This air supplied turbine produced 72 W of shaft power. To address the challenge of high speed operation, hybrid ball bearings were used [24]; these hybrid ball bearings were tested separately up to 800,000 rpm. Here, the challenge of fabricating the aerodynamically designed components with small features was addressed using a mold shape deposition manufacturing (SDM) process.

At Tohoku University [13], research was conducted on demonstrating a 100 W gas turbine. As part of this effort, a miniature radial turbine was designed and fabricated. The

operation of the turbine was demonstrated as part of a turbocharger unit. The challenge of operating at high speed was addressed using hydro-inertia gas bearings [13]. 5-axis micro-milling technology was employed to fabricate the 3-dimensional turbine blades, required to achieve high efficiency.

Table 1-2 summarizes the characteristics of the turbogenerator units found in the literature that produce electric power approximately in the 1 W – 100 W range. The teams at MIT/GIT and at KUL utilized an axial turbine. The MIT/GIT team coupled an off-the-shelf dental drill turbine with a custom designed axial-flux permanent-magnet synchronous MEMS generator. This turbogenerator demonstrated a net electric power output of 8 W at 305,000 rpm. The main challenges of containing the brittle rotor magnet material, and maximizing generator rotor speed, were addressed by a tight-fit containment hoop and by choosing samarium cobalt (SmCo) as magnet material. The challenge of implementing a compact stator winding was addressed by electroplating the winding in place using MEMS fabrication technologies. The team at KUL coupled a custom-designed axial turbine to an off-the-shelf generator and tested this up to 160,000 rpm, generating 16 W electrical power output. The low pressure ratio, 10 mm diameter axial turbine design resulted in high blade profile losses and high exit losses. The main challenge of manufacturing the axial turbine was addressed by using an electro-discharge machining (EDM) process.

A team at ETH, Switzerland, designed and fabricated a 100 W, 500,000 rpm generator, which was coupled to a 10 mm diameter micro-machined off-the-shelf radial turbine with a 590 um blade span. This turbogenerator was operated at 490,000 rpm, with 150 W net electric power output. The main challenge of reducing generator losses at high speed operation was addressed by optimizing the winding design and the stator core material. Rotor integrity at high speed was ensured by employing a titanium sleeve containing the magnet core.

Important to note is that the 50 W to 100 W turbine powers are achieved at pressure ratios near 2. The research in this thesis is aimed at designing a turbine at similar power levels but at pressure ratios of 5 – 6. This yields a major challenge in the turbine design which is the focus of this thesis. Four common themes can be identified from the previous work.

Generator choice and design: The generator of choice is a permanent-magnet synchronous machine. Furthermore, generator rotor integrity at high speed requires a containment hoop to reduce centrifugal stresses in the brittle rotor magnet material. Only

17

custom designed generators with containment hoops are able to achieve speeds above 100,000 rpm [16]. At high speed operation, rotor and stator losses require a design optimization, and an appropriate choice of the material.

Bearing technology: To ensure high speed operation, either hybrid ball bearings [24] or air bearings are used, as reported in [13], [21] and [32]. The trade-off is between the simplicity and availability of hybrid ball bearings and the longer lifetime of air bearings. For a given rotational bearing technology, the maximum speed that bearings can support depends on the DN number, where D is the diameter of the bearing (in mm) and N is the rotation rate in rpm. Conventional ball bearings achieve DN numbers of 2,000,000 to 3,000,000. High speed hybrid bearings manufactured by Myonic [24] can achieve DN numbers as high as 4,000,000. These bearings have higher DN numbers than their conventional counterparts because their ceramic balls match the ring material, the cage design reduces energy loss in the bearing, and dry lubrication minimizes the need for external lubrication. Air bearings provide an alternative option. They levitate the rotor by air pressure, either generated with an external supply (hydrostatic bearings) or by the motion of the rotor (hydrodynamic and air foil bearings). They have low friction losses and a longer lifetime. The disadvantage is that they are not yet commercially available. The details of an advanced micro gas bearing design can be found in [32]. For the speed range required here, hybrid ball bearings are preferable due to their simplicity. Thus, the turbogenerator design in this thesis will adopt existing hybrid ball bearings.

Turbine manufacturing technology: The minimum feature size is critical, and set by the manufacturing technology. Three technologies have been demonstrated successfully: micro-milling, SDM, and DRIE, yielding minimum feature sizes of 300 um, 200 um, and 10 um respectively. The 1 W to 100 W power range is at the intersection of two trends: existing meso-scale designs are scaled down by advancing conventional manufacturing technologies, and power MEMS are scaled up using new manufacturing technologies. While demonstrated technology is preferable when reliability is a design goal, certain constraints may require a new approach. Applied to the design problem studied in this thesis, the following conclusions can be drawn. The generator has to be custom-designed, and a meso-scale generator is preferable to a MEMS generator due to the higher demonstrated maximum rotor speed. Furthermore, the

minimum turbine blade span manufacturability limit imposed by micro-milling requires a MEMS manufacturing technology for smaller blade spans.

Turbine architecture: The options are single-stage versus multi-stage turbine, and radial versus axial flow machines. Most turbines are of the single-stage, radial inflow type. The radial turbines can operate at higher pressure ratios than the axial turbines and yield less complexity, as will be discussed in Section 2.5.1.

1.3. Challenges for a 50 W Turbogenerator Design

The blade manufacturability constraint and low turbine mass flow at high pressure ratio requirement constrain the turbine design and pose an unconventional turbomachinery problem. Moreover, the integrated generator design yields a challenging system design problem, since generator stress limitations ask for a low-speed design, whereas the low turbine mass flow and manufacturing considerations require a high speed design. The design requirements and considerations can be summarized as follows.

Minimum mass flow consumption: To minimize consumed mass flow for a 50 W turbogenerator power output, high specific turbine work is desired. This requires high turbine pressure ratio and turbine adiabatic efficiency, and a relatively low flow area. To achieve the required turbine tip velocities while relieving the blade span constraint, high turbine shaft speeds are desired.

Turbine manufacturing constraints: The minimum feature size is set by the choice of manufacturing technology. The critical feature size is the blade span and in light of the low mass flow requirement, MEMS based approaches using DRIE become attractive.

Generator centrifugal stress: Since an integrated generator and turbine have the same shaft speed, the maximum allowable turbine speed is constrained by the allowable generator centrifugal stress limit. Thus, lower shaft speeds are desired. It is evident that the generator and turbine design considerations yield opposite trends, making the integrated turbogenerator design a challenging endeavor.

1.4. Research Objectives and Goals

The goals of this thesis are to explore the design space for a 50 W turbogenerator, to determine the major constraints and design trade-offs, and to carry out an in depth analysis and the design of a turbogenerator. The 50 W design requires a mass flow as low as possible while maintaining a supply pressure of 5-bar. Chapter 2 presents the turbogenerator design space and a first-principles based analysis combined with empirical correlations to identify the limiting technologies and major trades between the turbine and generator design. Chapter 3 presents the design of a high specific-work, low specific-flow radial turbine required to meet the design goals and details a high-fidelity assessment of the turbine performance using 3D CFD. Chapter 4 summarizes the key findings and the recommendations for future work.

Chapter 2.   Turbogenerator System Analysis

2.1.   Conceptual Layout of a Turbogenerator System

The proposed turbogenerator system consists of the major elements shown in Figure 2-1: a shut-off and throttle valve, a turbine that drives a generator, power electronics, a control system, and a muffler to quiet the exhaust air. The shut-off and throttle valve modulate the air flow to the turbine and set the turbine inlet total pressure, which in return determines the useful turbine work and the turbine mass flow. The power electronics transform the output of the generator to a form compatible with the load, while the control system modulates the air according to the power demand and ensures safe operation.
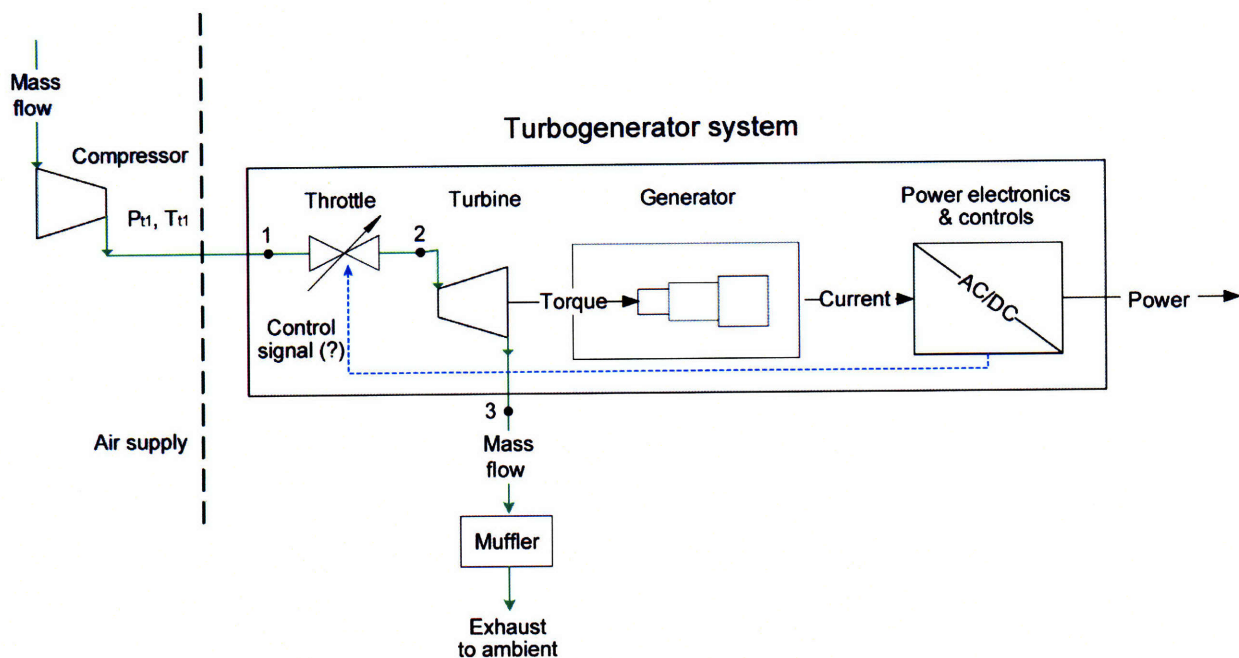
Figure 2-1: System layout of the proposed turbogenerator system.

2.2.   Low Mass Flow Requirement

In this section, the low mass flow requirement and its design implications are discussed in detail. First, through a zero-order thermodynamic analysis, the required system characteristics are investigated. Second, the targeted mass flow range is identified as a function of efficiency and pressure ratio. Third, for the low mass flow requirement, the necessary

turbine dimensions and design features are assessed, identifying the key turbine limitation, blade manufacturability.

Figure 2-2 shows the process of converting the energy stored in compressed air to useful work employing thermodynamic coordinates in an enthalpy-entropy diagram. The change in stagnation enthalpy, Δh_t, is equivalent to the specific shaft work of the turbine, the useful work. The change in entropy, Δs, indicates dissipation and irreversibility, the lost work. As Figure 2-2 indicates, the throttle valve reduces the available work by decreasing the total pressure, creating entropy. Downstream of the valve, the turbine extracts useful work from the compressed air. Due to irreversibilities in the turbine during the expansion process, entropy is generated, which further reduces the useful work. Thus, given a turbine design and technology, the highest turbine pressure ratio should be utilized in order to maximize useful work and to minimize lost work. Ideally, the throttle valve should therefore be operated only as a safety shut-off valve. For a set power demand, reducing consumed mass flow is equivalent to increasing specific work, so a low mass flow is equivalent to high efficiency. This yields the following design implications. First, component efficiency must be maximized. Second, since the air must not be throttled, the turbine must be designed to operate at the highest possible pressure ratio.
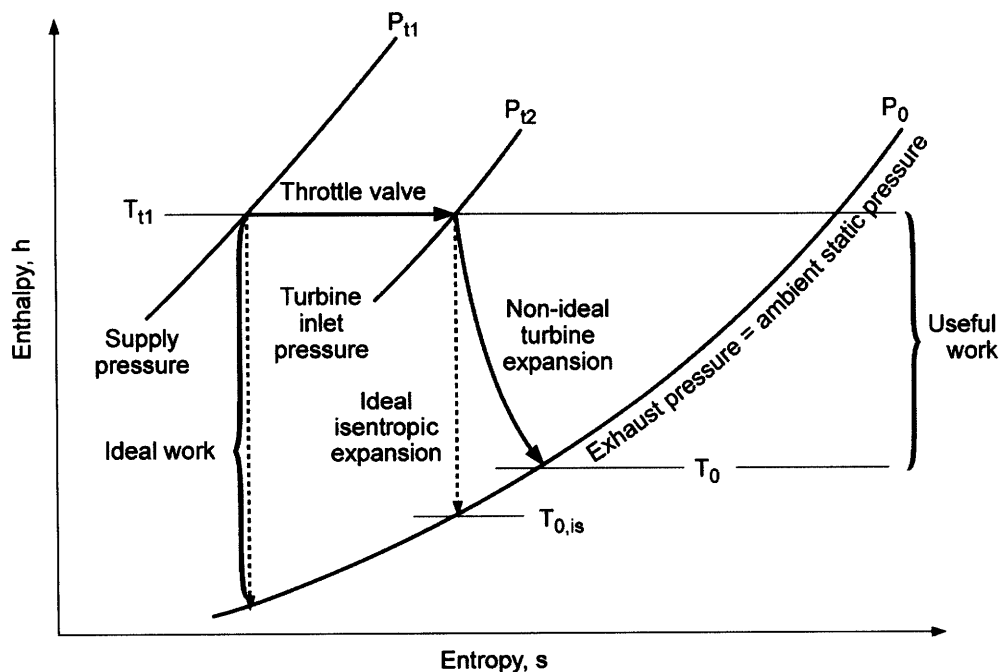
Figure 2-2: Conversion of compressed air to useful work.

From the 1st law of thermodynamics and the definition of adiabatic turbine efficiency, the net electric power output of the turbogenerator can be written as a function of mass flow, component efficiencies, and turbine total-to-static pressure ratio as

$$P_{out,el} = \dot{m} \cdot w_t = \dot{m} \cdot \eta_T^{ad} \cdot c_p \cdot T_{t,2} \cdot \left(1 - PR_{t-s}^{\frac{1-\gamma}{\gamma}}\right) \cdot \eta_{GE} \cdot \eta_{PE}. \tag{2-1}$$

Based on Equation (2-1), Figure 2-3 shows contours of specific work (power divided by mass flow) as a function of turbine efficiency and turbine total-to-static pressure ratio. In this analysis a generator efficiency of 80 %, a power electronics efficiency of 90 %, and an air inlet total temperature of 300 K are assumed, typical for a device operating near the 50 W power level. More details can be found in Section 2.7. Figure 2-3 can be utilized to determine the mass flow for a set amount of turbogenerator power, pressure ratio and turbine efficiency. For a given power output of 50 W and a 5:1 pressure ratio, the mass flow ranges between 1 and 2.5 g/s for 70 % to 30 % adiabatic turbine efficiency. The required mass flow will have an important impact on turbine blade design.
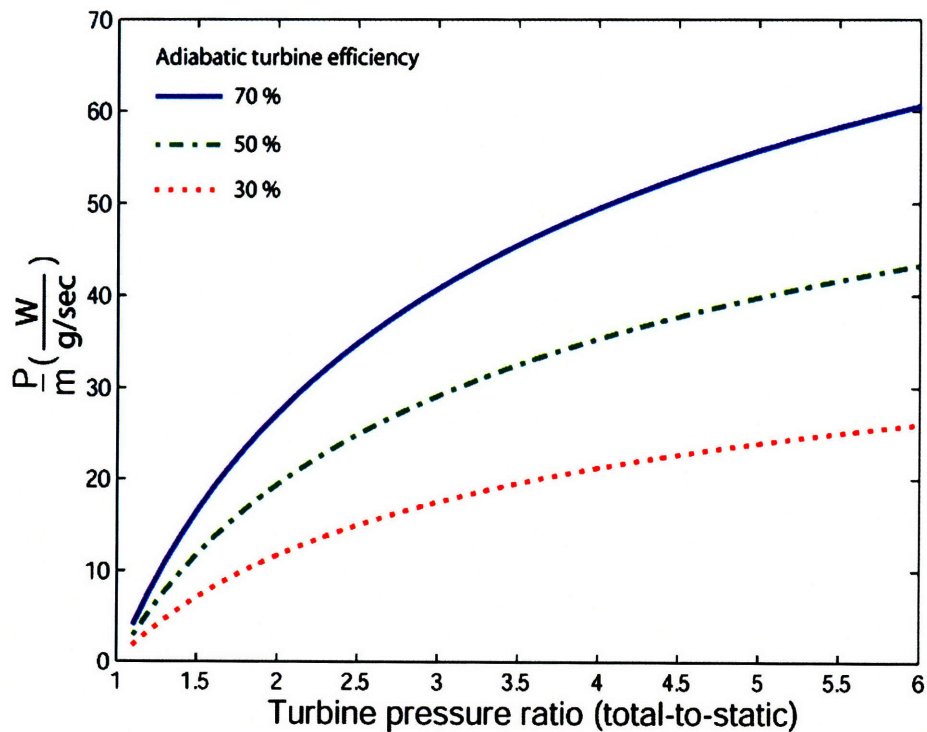
Figure 2-3: Power divided by mass flow versus turbine pressure ratio for different adiabatic turbine efficiencies, assuming generator efficiency of 80 %, power electronics efficiency of 90 % and an air inlet total temperature of 300 K.

For a radial inflow turbine, the flow area can be written as

$$A = 2\pi \cdot R \cdot h, \tag{2-2}$$

where R is the turbine radius and h is the blade span. Hence, for constant flow area, the blade span decreases as turbine radius increases. Assuming an inlet total pressure of 5 bar, a typical stator outlet flow angle of 75 degrees (high specific work) and choked flow, Figure 2-4 depicts the resulting blade span for different turbine radii and mass flows for a turbogenerator power output of 50 W. Furthermore, the minimum blade span for micro-milling manufacturing is indicated as a solid line. For a mass flow of 1 g/s and a turbine radius of 2 to 10 mm, the blade span ranges between 50 and 250 um. The analysis shows that the combined requirement for 50 W power output and low mass flow yields turbine blade spans below the conventional blade manufacturability limit for turbine radii larger than ~2 mm. Hence, an alternative manufacturing technology is required for a low flow, 50 W turbine. Two MEMS manufacturing options are discussed in Section 2.6.2, mold SDM and DRIE. Furthermore, this implies that the low ratio of blade span to turbine diameter yields turbine designs with increased end-wall losses, reducing the adiabatic turbine efficiency.
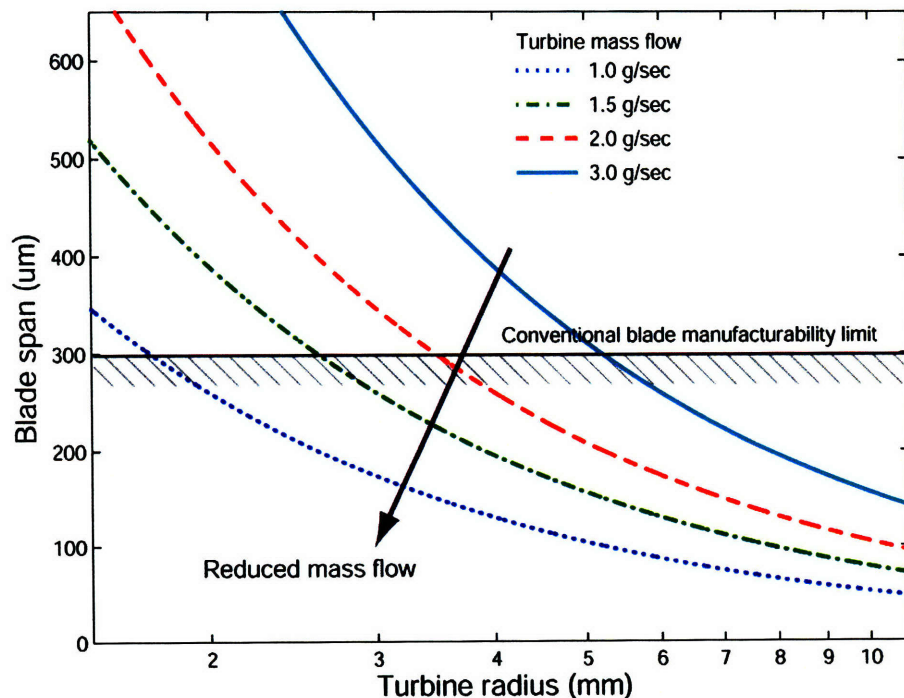
Figure 2-4: Blade span versus turbine radius for different mass flows, assuming an inlet total pressure of 5 bar, a stator outlet flow angle of 75 deg and choked flow for 50 W turbogenerator power output.

24

2.3. Design Requirements and Challenges

The primary challenge is the integrated turbine and generator design. The analysis carried out in Section 2.2 shows the following. To achieve a low mass flow for a set demand of turbogenerator power output, the turbine specific work must be high and the flow should not be throttled, taking advantage of the high pressure ratio of the air supply. Furthermore, the conventional micro-milling process imposes a blade manufacturability limit. For a constant flow area, the blade span is increased at lower turbine radii, and, for a given turbine architecture, the high specific turbine work requires a certain tip speed to meet the shaft power requirement. Thus, small turbine radii yield high shaft speeds. However, generator rotor balancing, mechanical stress and bearing considerations limit the maximum generator speed. High generator speeds require additional design efforts, as detailed in Section 2.7.2. Therefore, the integrated turbine and generator design must balance the blade manufacturability and generator speed constraints: the higher the rotor shaft speed, the less challenging the turbine design and the more challenging the generator design, and vice-versa. Figure 2-5 illustrates the relationship between structural integrity considerations and blade manufacturability.
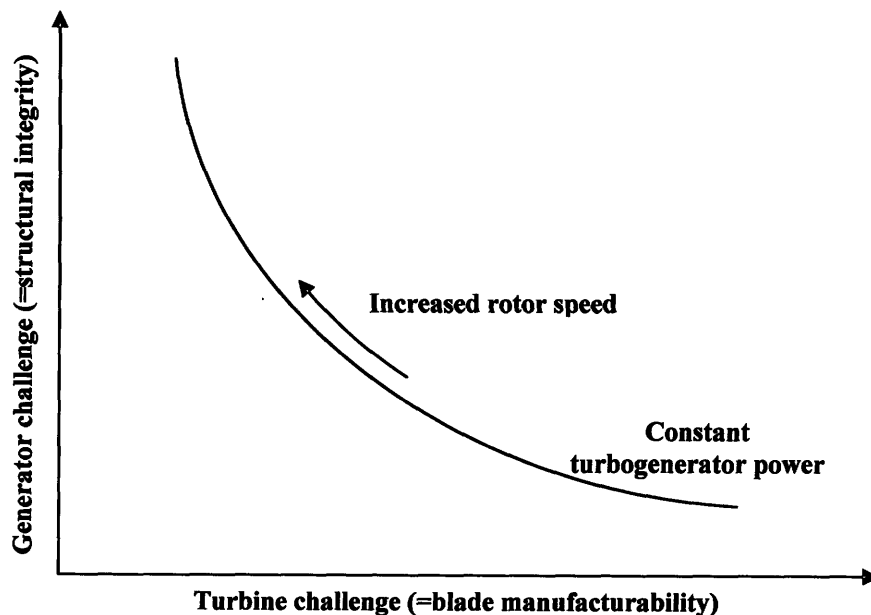
Figure 2-5: Illustration of trade-off between turbine challenge and generator challenge at constant turbogenerator power output.

2.4. Assessment Methodology

The challenge is to design an integrated turbogenerator system. Since turbine and generator are on the same shaft, torque and angular speeds are identical; this tightly couples their aerodynamic and electromagnetic design. First, based on first principles, the system architecture is discussed and investigated with respect to the design requirements. Next, the major constraints on the component architectures are identified. Then, an analytical model along with suitable approximations is given to scale the performance as a function of design. The two sets of design constraints and scaling laws are combined to investigate the integrated turbogenerator system. Finally, the insight gained is discussed and a preliminary design is presented.

2.5. System Architecture

To begin its development, the system architecture is discussed in this section based on first principles. The turbine architecture selection criteria are based on low specific-flow, high specific-work, blade manufacturability, turbine adiabatic efficiency and mechanical simplicity. The generator architecture selection criteria are efficiency, compactness and structural integrity at high speed. The goal is to define a system architecture that best meets these individual requirements.

2.5.1. Turbine Architecture

There are two distinct turbine architectures possible for this application: a radial inflow turbine or an axial flow turbine, as illustrated in Figure 2-6.
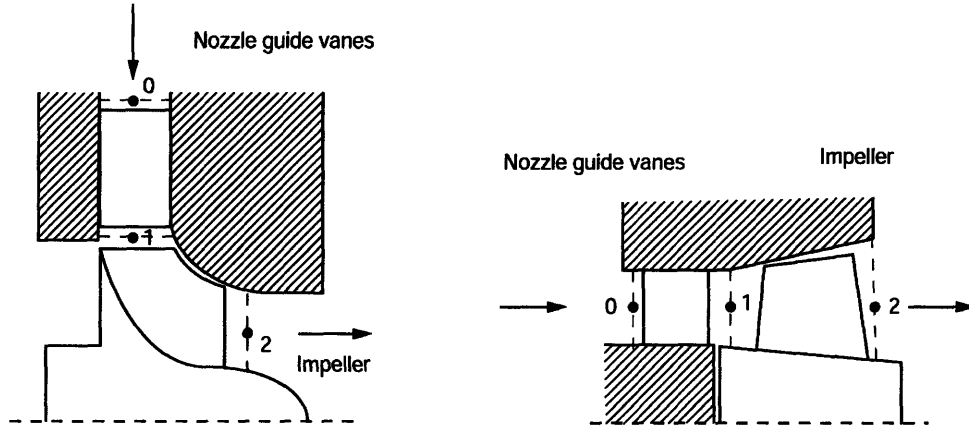
Figure 2-6: Comparison between a radial (left) and an axial turbine stage (right).

In comparison to axial turbines, radial inflow turbines have multiple advantages. Radial turbines have a smaller inlet area for the same rotor diameter due to their reduced blade span to tip radius ratio. A typical axial turbine hub-to-tip ratio of 0.4 to 0.6 results in a larger blade span than in a typical radial turbine where the blade span-to-tip radius ratio is typically 0.1 to 0.3 [28]. Hence, radial inflow turbines are preferable for low specific-flow applications. As detailed in Section 2.7.1, Euler's turbine equation links specific shaft-work and velocity triangles through

$$w_t = \frac{1}{2} \cdot \left[\left(U_1^2 - U_2^2 \right) - \left(W_1^2 - W_2^2 \right) + \left(C_1^2 - C_2^2 \right) \right], \tag{2-3}$$

where U is the rotor speed, C is the absolute velocity, and W is the relative velocity. Station 1 is at the rotor inlet and station 2 is at the rotor outlet. For axial turbines, where changes in mean-line radius are negligible and hence $U_1 \approx U_2$, little or no contribution to the specific shaft-work is obtained from the centrifugal effect captured in the first term. However, for radial turbines, where $U_1 > U_2$, the change in rotor velocity contributes significantly to the specific work. Hence, radial turbines achieve a higher pressure ratio for the same rotational speed due to the centrifugal effect [7]. Thus, radial turbines are preferable for high specific-work applications and are used when a more compact power source is needed.

In addition, radial turbines are relatively simple to manufacture (typically single cast) and robust [30]. In axial machines, the blade angles over the blade span vary if the work coefficient is kept constant. Hence, blades in an axial machine are twisted and require special

manufacturing technology. This is deemed difficult to implement at the level of miniaturization required here. This judgement is corroborated by findings reported in [25] and [34].

The advantage of a multi-stage design is higher efficiency because rotor tip speed can be lowered for a set amount of specific work; the disadvantage of a multi-stage design is increased complexity. Since one of the goals here is to keep the design simple and compact, a single-stage is preferable in order to avoid complex rotor designs and large turbine diameter. As a consequence, a high specific-work coefficient is required.

An alternative axial design that would meet the work requirement is a high flow and low pressure ratio configuration, reported in Appendix B. To reduce the pressure ratio, the turbogenerator would have to be placed in series with another load. Due to the low pressure ratio across the axial turbine resulting from this configuration, the mass flow required to meet the turbogenerator power goal is much increased. Furthermore, ducting losses become an important consideration, and the overall design becomes inefficient.

In summary, a single-stage radial turbine is desired for this high pressure ratio, low flow 50 W turbogenerator application. The remainder of this thesis is focused on the detailed design of such a device.

2.5.2. Generator Architecture

Permanent-magnet synchronous generators are more efficient and power-dense than other generators at small sizes because permanent magnets provide the same magnetic flux density independent of size, whereas it is increasingly difficult from a thermal viewpoint to produce a given flux density from a rotor winding as size decreases because Ohmic losses in the rotor windings require more cooling surface than is available. Two distinct generator shapes are possible for this application: the traditional axial "cylindrical-shaped" rotor and the disk-shaped "pancake" rotor, as illustrated in Figure 2-7.
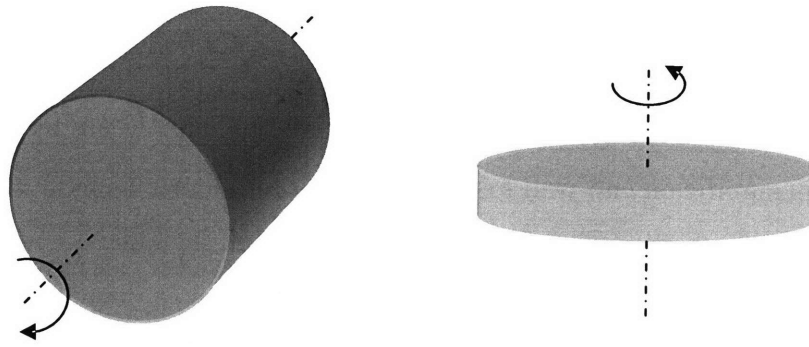
Figure 2-7: Comparison of cylindrical (left) and pancake (right) generator rotor configurations.

A cylindrical geometry is assumed so that all magnets are at the maximum lever arm, which makes the generator compact. In addition, this geometry places no magnetic load on the bearings. For cylindrical generators, centrifugal stress sets the maximum rotor tip speed. This tip speed can be increased by using a containment hoop. In the study reported here, a cylindrical permanent-magnet synchronous generator with a containment hoop is assumed.

2.6. Overview of Constraints

As part of the assessment, the major constraints of the turbine and generator architectures are identified in this section. The main design variables are turbine and generator diameter size and shaft speed as a function of turbogenerator power output. Manufacturing constraints and limitations are related to off-the-shelf availability of components and current manufacturing standards.

2.6.1. Design Constraints

Based on results from [2] and [33], it is hypothesized that, as the turbine gets smaller in diameter, there is a diameter for which the flow transitions from turbulent to laminar, such that turbine adiabatic efficiency deteriorates significantly. For the shaft speeds considered here, the critical turbine radius is approximately 1 mm to 3 mm. This estimate is corroborated by previous work on micro engines [14]. Thus, a 2 mm turbine radius will be assumed to be the minimum turbine radius in the study discussed here.

Based on the computational results presented in Appendix C, it can be concluded that the minimum allowable blade span is constrained by aerodynamic considerations. The study shows that a 100 um passage height, with an 80 um blade span and 20 um tip clearance gap in the rotor, results in significant end-wall losses, yielding a turbine adiabatic efficiency of 28 %. As previously outlined, a high component efficiency is desired, such that a 100 um tall gas path is assumed to be the limiting blade span.

The allowable centrifugal stress in the turbine rotor limits the maximum turbine rotor tip speed. Assuming an axisymmetric, solid rotating disc under elastic deformation, the limiting tip speed can be written as

$$(R \cdot \Omega)^2 = \frac{8}{(3+\nu)} \cdot \frac{\sigma_{max}}{\rho}, \qquad (2\text{-}4)$$

where σ_{max} is the maximum mechanical stress, ρ is the material density, and ν is the Poisson coefficient. The higher the strength-to-density ratio of the material, the higher the limiting tip speed. The tip speed is limited to 300 m/s for plastic, 500 m/s for aluminum and 700 m/s for titanium. However, efficiency considerations require sub-sonic turbine rotor operation; for cold air the tip speed should stay well below 330 m/s. Therefore, if silicon nitride or a metal is used, the turbine material stress limit is not a relevant constraint.

For example, assuming zero exit swirl, a flow coefficient of ϕ = 0.5, and a constant

axial velocity through the stage, the work coefficient, $\Psi = \frac{w_t}{U^2}$, for a typical reaction turbine

equals one, and the work coefficient for a typical impulse turbine, or zero reaction turbine, equals two, as illustrated by the velocity triangles in Figure 2-8.
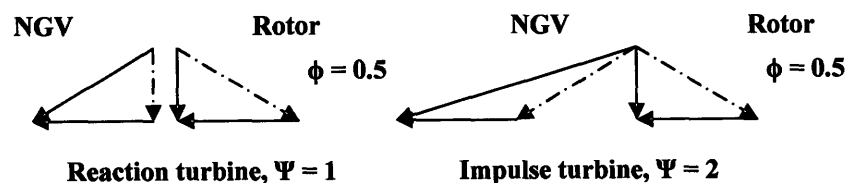
Figure 2-8: Velocity triangles for typical reaction and impulse turbines.

Using the 1st law of thermodynamics, the definition of turbine adiabatic efficiency and the definition of work coefficient, the turbine pressure ratio can be written as a function of rotor tip Mach number, work coefficient and rotor efficiency

$$PR = [1 - \frac{\gamma - 1}{2} \cdot \frac{\Psi}{\eta^{ad}{}_T} \cdot M_{U1}{}^2]^{\frac{-\gamma}{(\gamma-1)}} .$$ (2-5)

To avoid shock losses, the stage should be operated well below sonic conditions. Tip Mach number of 0.9 and a turbine adiabatic efficiency of 50% are assumed to estimate the highest possible pressure ratio if a reaction turbine were used. This yields a turbine pressure ratio of 4.5. Thus, in order to operate at supply pressure ratios of 5-6 with a single-stage design, a low-reaction turbine design is required.

The generator length should be approximately five times the magnet thickness or greater otherwise the magnetic fields begin to fringe outward in the axial direction and the shear stress and efficiency decrease rapidly, as mentioned in [12]. Since the smallest allowable generator magnet thickness is assumed 800 um due to manufacturing constraints [18], the generator length becomes 5 mm. Because high component efficiency is required, this generator length is assumed to be the shortest possible generator length considered in this study.

For a generator without a containment hoop, the maximum rotor tip speed is limited by the allowable mechanical stress in the magnet material. Assuming an axisymmetric, solid rotating disc under elastic deformation, the limiting tip speed becomes

$$(R \cdot \Omega)^2 < \frac{8}{(3+\nu)} \cdot \frac{\sigma_{max}}{\rho},$$ (2-6)

where σ_{mas} is the maximum allowable mechanical stress of the magnet material, ρ is the magnet material density, and ν is the Poisson coefficient respectively. For a typical permanent-magnet material with $\rho = 8{,}500 \frac{kg}{m^3}$, $\nu = 0.3$, and $\sigma_{max} = 25$ MPa, the tip speed is 80 m/s. This is too low and so external containment is required.

The magnets can be contained within a containment hoop. In this case hoop failure limits the maximum generator rotor tip speed. This hoop must be much thinner than the magnets to preserve good magnetic performance. A detailed model to estimate the burst speed can be found in [31], but a first order estimate of the limiting rotor tip speed is

$$\left(R \cdot \Omega \right)^2 < \frac{\sigma_{max,hoop}}{\rho_{magnet}} \cdot \frac{\text{Hoop thickness}}{\text{Magnet thickness}} \cdot \frac{1}{SF} , \qquad (2\text{-}7)$$

written as a function of mass density of the magnet material (commonly Sm2Co17 or NdBFe depending on the temperature), and the strength and thickness of the hoop; SF is a safety factor. For a typical magnet density of 8,500 kg/m^3, a required minimum hoop-to-magnet thickness ratio of 1:8, a safety factor of 1.5, and a containment ultimate material strength of 1500 MPa for Kevlar, the limiting rotor tip speed is 120 m/s. For Inconel with a material ultimate strength of 2500 MPa, the limiting rotor tip speed is 155 m/s. For titanium with a material ultimate strength of 3500 MPa, a limiting rotor tip speed of 180 m/s can be achieved. The maximum tip speed in combination with the minimum generator rotor diameter determines the maximum shaft speed, which in turn is important for the turbine design because low turbogenerator flow considerations shift the design towards high rotational speeds.

The maximum allowable rotor magnetic shear stress is limited to roughly 35 kPa (5 psi) [22]. This limit depends on magnet properties, magnetic core saturation, and reasonable stator cooling limitations. The magnetic shear stress could be increased through forced air cooling to 70 kPa (10 psi) [22].

2.6.2. Manufacturing Constraints

Current manufacturing technology sets the minimum magnet thickness to approximately 800 um [18] for high strength magnets. Furthermore, the difficulty of assembling the magnets for small rotors sets the smallest possible rotor diameter to approximately 4 mm.

In a radial turbine, micro-milling manufacturing technology limits the shortest blade span to 300 um [34]. This is set by the manufacturing precision of micro-milling machines and structural integrity considerations set by the fillet radii at the blade root where stress concentrations can occur. Since conventional manufacturing methods limit the blade to 300 um, an alternative manufacturing approach is needed to enable shortened blade spans. The mold SDM process in combination with ceramic gel-casting can achieve feature sizes as small as 200 um [33]. Silicon etching technology offers a solution for blade spans below 200 um. Deep reactive ion etching (DRIE) technology was successfully used in the Micro-Engine Project at

MIT [14]. This process consists of placing a mask on a wafer, and removing the exposed material through etching. The etch depth and their profiles are controllable. The result is a planar geometry with two-dimensional features [14]. Figure 2-9 shows a scanning electron microscope (SEM) image of an etched silicon micro turbine, with a 4.2 mm rotor diameter and 0.4 mm blade span [26].
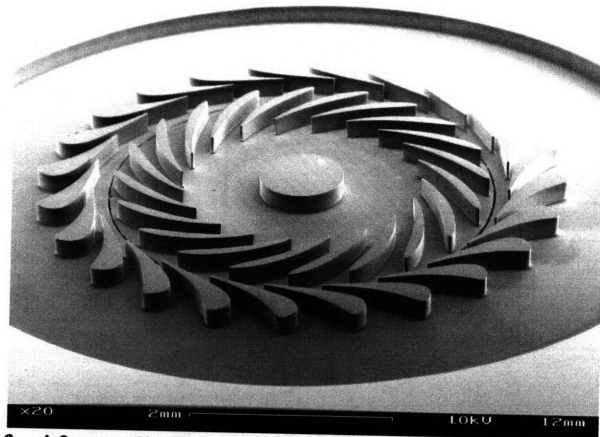
Figure 2-9: SEM picture of a 4.2 mm diameter silicon rotor, 60 Watt turbine with 0.4mm blade span [26].

In conclusion, both the turbine and the generator designs are constrained by rotor diameter and shaft speed limits. Blade manufacturability and structural integrity considerations form the two major limitations of the design.

2.7.   Turbogenerator Performance Assessment

A 1st principles based model along with suitable assumptions is presented in order to assess the turbogenerator performance as a function of the key design parameters: rotor shaft speed and device diameter at a set level of turbogenerator power output.

2.7.1. Scaling of Radial Turbines

A radial turbine is comprised of two major components: a set of stator blades (often referred to as nozzle guide vanes) and a set of rotor blades (often referred to as impeller blades), as shown in Figure 2-10. Two factors determine the shaft power output of a turbine: mass flow

33

and specific shaft-work. Both factors can be modeled as a function of rotor diameter and shaft speed. The goal here is to develop a set of scaling laws that can be used to explore the design space.
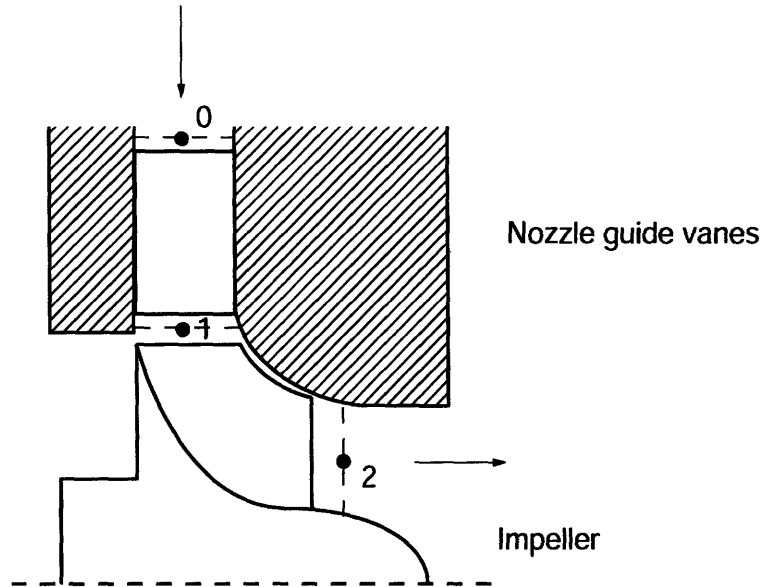
Figure 2-10: Schematic of radial turbine stage.

The corrected mass flow per unit area through a radial turbine can be expressed in terms of the inlet total pressure p_t and total temperature T_t, the flow area A, the specific heat ratio γ, and the local Mach number M at the throat of the nozzle guide vanes as

$$\frac{\dot{m} \cdot \sqrt{\frac{R}{\gamma} \cdot T_t}}{p_t \cdot A} = \frac{M}{\left(1 + \frac{\gamma - 1}{\gamma} \cdot M^2\right)^{\frac{\gamma+1}{2 \cdot (\gamma-1)}}}. \qquad (2\text{-}8)$$

The flow area based on the rotor radius R and the blade span h is given by

$$A = 2 \cdot \pi \cdot R \cdot h. \qquad (2\text{-}9)$$

For pressure ratios above the critical pressure ratio of 1.89, the flow is choked and Equation (2-8) simplifies to

34

$$\frac{\dot{m}\cdot\sqrt{\dfrac{R}{\gamma}\cdot T_t}}{p_t \cdot A} = 0.58.$$ (2-10)

The mass flow per unit area is thus proportional to the inlet total pressure and the inverse of the square of the inlet total temperature. The flow coefficient ϕ, defined in Equation (2-11), can be written as

$$\phi = \frac{\dot{m}}{2\pi \cdot h \cdot R \cdot \rho \cdot U},$$ (2-11)

and can be related to the velocity triangles. At the rotor inlet, station 1, the flow coefficient becomes

$$\phi_1 = \frac{C_{1n}}{U_1} = \frac{\cos(\alpha_1)}{\sin(\alpha_1) - \cos(\alpha_1)\cdot\tan(\beta_1)}$$ (2-12)

Typical values for flow coefficients can vary from 0.3 to 0.7, as reported in [35].

From the 1st law of thermodynamics for steady, adiabatic flow, the specific shaft-work is equal to the change in total enthalpy

$$w_t = \Delta h_t.$$ (2-13)

For a calorically perfect gas, the change in total enthalpy is related to a change in total temperature by

$$\Delta h_t = c_p \cdot \Delta T_t,$$ (2-14)

such that, with the definition of turbine adiabatic efficiency

$$\eta_T{}^{ad} = \frac{1-\tau}{(1-\pi)^{\frac{1-\gamma}{\gamma}}}$$ (2-15)

the change in total enthalpy then can be expressed as

$$\Delta h_t = \eta_T{}^{ad}\cdot c_p \cdot T_{t2}\cdot\left(1-\left[\frac{p_{t2}}{p_0}\right]^{\frac{1-\gamma}{\gamma}}\right).$$ (2-16)

The change in enthalpy is a non-linear function of the pressure ratio across the turbine and increases with an increasing pressure ratio, everything else equal. Using the Euler turbine equation, the specific shaft work can be linked to the velocity triangles through

$$w_t = \Delta(UC_\theta),$$ (2-17)

where C_θ is the tangential component of the absolute flow velocity and U is the wheel speed. The work coefficient is then defined as

$$\Psi = \frac{w_t}{U_1^2} = \frac{\Delta(UC_\theta)}{U_1^2},$$

(2-18)

where U_1 is the wheel speed at rotor inlet. Assuming no exit swirl, and using relationships from the velocity triangles, the work coefficient for an ideal rotor can be expressed in terms of the absolute flow angle α and relative flow angle β at the rotor inlet according to

$$\Psi = \frac{\sin(\alpha_1)}{\sin(\alpha_1) - \cos(\alpha_1) \cdot \tan(\beta_1)}.$$

(2-19)

Typical values for the work coefficient of radial machines vary from 0.8 to 1.2, with 0.85 known to yield optimum efficiency in conventional single-stage radial inflow designs [3].

At small scale, end-wall boundary layers yield increased blockage and increased viscous losses. Typical small scale turbine adiabatic efficiencies can range between 20 % and 70 % as reported in [5], [13], [20], [25], and [33] for 4 mm to 14 mm diameter turbines. For now this study assumes 30 % turbine adiabatic efficiency, although, for 50 W operation of a planar turbine geometry, a 50 % turbine adiabatic efficiency can be expected as reported from computational results in [14]. High fidelity flow field computations are conducted on a candidate design to assess this assumption. These results are reported in Section 3.5.

2.7.2. Scaling of Cylindrical Generators

Building the axial-shaped generator from the rotor core outwards, there is first a steel core, then magnets, then optionally a containment hoop, then an air gap, and finally the stator core as Figure 2-11 illustrates. In this figure, it is assumed that the stator windings are set in the slots within the stator core, hence they are not shown. Since the main focus is on the scaling of generator power with speed and size, the stator scaling is not further discussed in this thesis because only the rotor dimensions interact with the turbine.

36
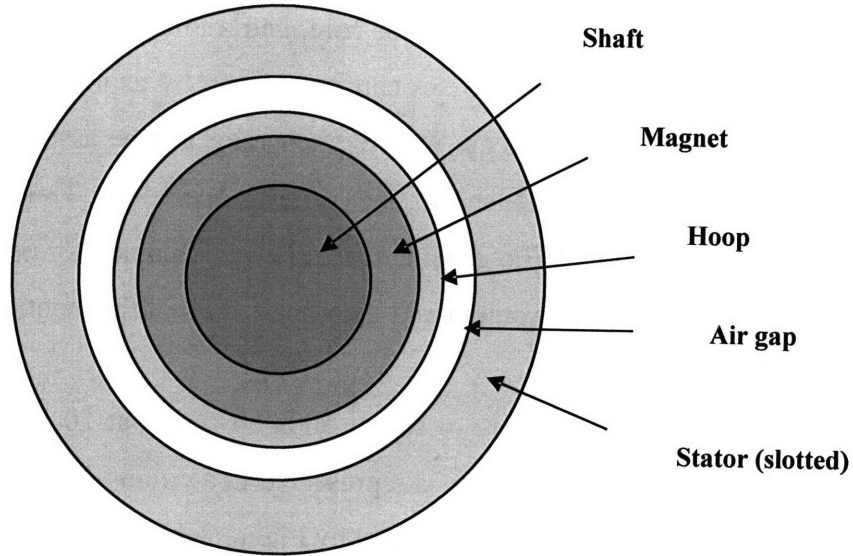
Figure 2-11: Cross section of cylindrical generator.

The power input P_{in} of a permanent-magnet, cylindrical-shaped generator is the product of torque T and speed Ω, hence

$$P_{in} = T \cdot \Omega . \qquad (2\text{-}20)$$

The torque produced by an cylindrical-shaped machine can be predicted to first order as the product of generator efficiency η_{GE}, magnetic shear stress σ, the active surface area and the lever arm according to

$$T = \eta_{GE} \cdot \sigma \cdot (2 \cdot \pi \cdot R \cdot L) \cdot R . \qquad (2\text{-}21)$$

Hence, the generator power output of a generator is

$$P_{out} = \sigma \cdot (2 \cdot \pi \cdot R \cdot L) \cdot R \cdot \Omega \cdot \eta_{GE} . \qquad (2\text{-}22)$$

There are four major loss sources in the generator: Ohmic losses in the windings, eddy current losses in the windings of a slotless machine, eddy current losses in the stator core, and hysteresis losses in the stator core. All but the Ohmic losses result from a varying magnetic field caused by moving magnets; they are hence dependant on speed. Eddy current losses and hysteresis losses in the stator scale together typically as $\propto \omega^{1.8}$, and eddy current losses in the windings of a slotless machine scale as $\propto \omega^2$. Thus, it becomes increasingly difficult to design an efficient generator at higher speeds. To reduce losses at high speed operation, certain design measures are required: Litz wire can be used in the windings of a slotless machine, thin

37

laminations and ferrite can be used in the stator core, and a thick core made of ferrite can be used for the stator. Finally, the Ohmic losses can be reduced by using copper and optimizing the air gap size. If these requirements are met, the generator can be assumed to first order as 80% efficient even at high shaft speed and 50 W operation. This approximation is corroborated by results from [37]. The generator in [37] was designed for operation at 500,000 rpm and 100 W net electrical power output and incorporated all of the mentioned modifications, hence achieving 87 % efficiency.

If the very same generator were to run at 500,000 rpm, but 50 W, its efficiency will increase. To understand this, the generator is represented in a circuit diagram as a resistance in series with a load and power supply, as illustrated by Figure 2-12.
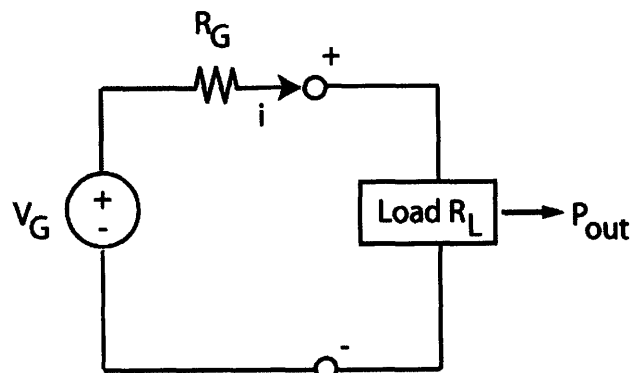
Figure 2-12: Illustration of circuit diagram.

The power output as function of generator resistance R_{GE}, load resistance R_L and terminal voltage V_{GE} can be written as

$$P_{out} = \left(\frac{V_{GE}}{R_{GE} + R_L}\right)^2 R_L,$$

(2-23)

and the power input as

$$P_{in} = \frac{V_{GE}}{R_{GE} + R_L} V_{GE}.$$

(2-24)

Generator efficiency is defined as ratio of power input to power output

$$\eta_{GE} = \frac{P_{in}}{P_{out}} = \frac{R_L}{R_L + R_{GE}}$$

(2-25)

and similarly

38

$$\left(1 - \eta_{GE}\right) = \frac{R_{GE}}{R_L + R_{GE}}. \tag{2-26}$$

Substituting the above equations into the definition of power output, the generator power output can be written as function of generator efficiency and the generator parameters phase resistance and terminal voltage

$$P_{out} = (\frac{V_{GE}}{R_{GE}}) \cdot \eta_{GE} \cdot \left(1 - \eta_{GE}\right). \tag{2-27}$$

Thus, for a specified generator phase resistance and constant terminal voltage at constant rotor speed, the efficiency increases for decreasing power output, as depicted in Figure 2-13.
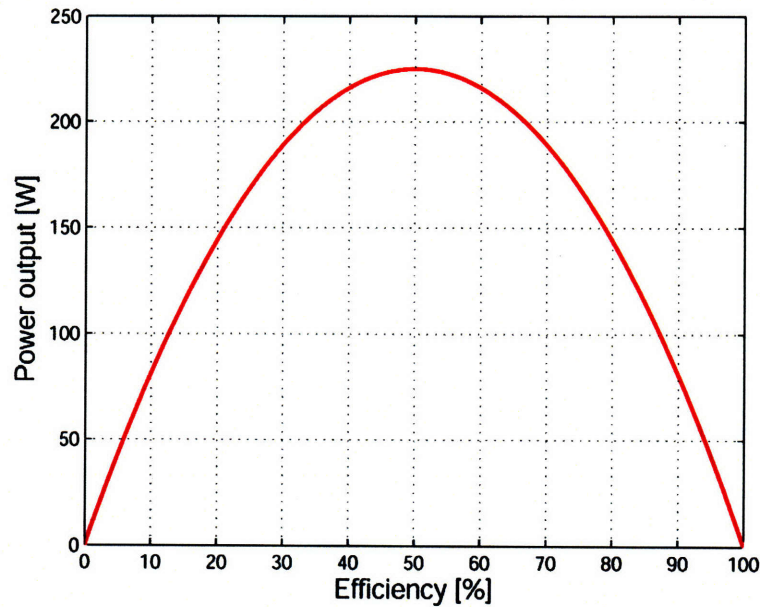
Figure 2-13: Power output versus generator efficiency at constant speed for generator reported in [37].

The expected electric frequency of the generator, based on the number of pole pairs and speed, defined as

$$\omega_{el} = \Omega \cdot n, \tag{2-28}$$

is on the order of $5 - 10$ kHz. Efficient power electronics have been demonstrated for an electric frequency of 20 kHz in [37]. Commonly, the power electronics efficiency is limited by cost rather than by physics. Hence, power electronics are assumed to first order as 90 % efficient.

2.8.   *Turbogenerator Design Space Exploration*

The objective here is to investigate the relationship between the turbine and generator design and to explore the 50 W, low flow turbogenerator design space. The turbine and generator are connected through a common shaft such that both components have the same shaft speed because a gear box is judged not to be a viable solution at the assumed size.

Figure 2-14 depicts the limitations of conventionally manufactured blades (limited to 300 um), and the effect of the desired turbogenerator power output level on rotor diameter and shaft speed. Two observations can be made. First, for a blade span of 300 um, it is not possible to achieve a 5:1 pressure ratio for 50 W turbogenerator power output. Second, as power increases, turbine pressure ratios of 5:1 become feasible. The key limitation is due to the low mass flow requirement and inherent blade span limitation. To relieve the blade manufacturing constraint, an alternative fabrication method is required for a 50 W, high specific-work turbine design.
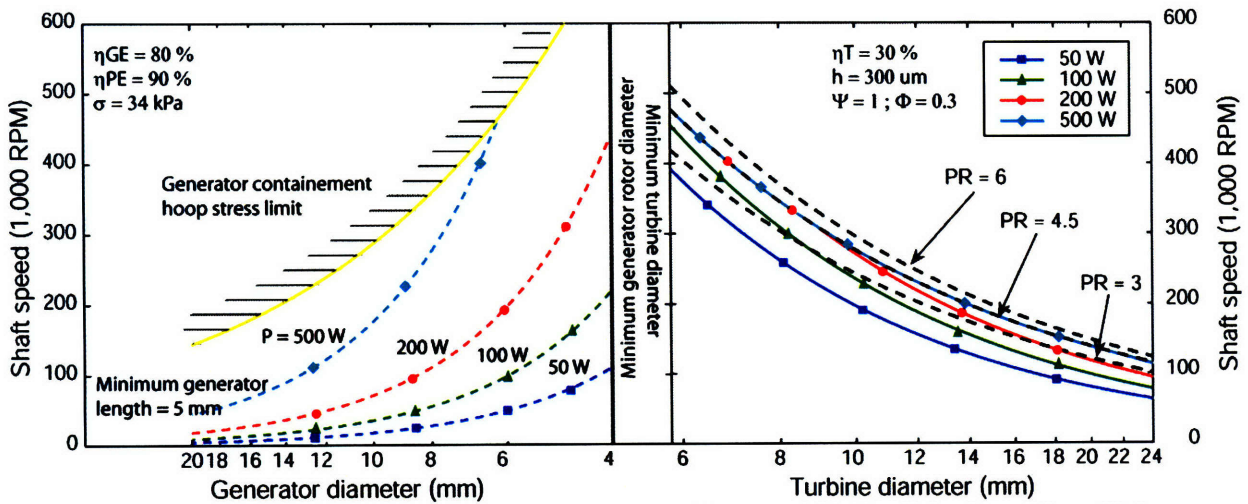
Figure 2-14: System chart for a turbine blade span of 300 um and 30 % adiabatic turbine efficiency.

The left-hand graph in Figure 2-14 displays contours of constant turbogenerator output power, derived from Equation (2-22), as a function of generator diameter and speed, assuming a shear stress of 5 psi, a generator efficiency of 80 %, a power electronics efficiency of 90 %, and a generator length of 5 mm. The generator design space is constrained by the smallest allowable generator rotor diameter dictated by manufacturing constraints and the maximum allowable generator rotor tip speed set by stress limitations in the containment hoop, derived

40

from Equation (2-7). For a set turbogenerator power output and generator diameter, increasing the rotor speed would require a shear stress reduction, derived from Equation (2-22), while decreasing the speed would require additional generator length. For a set turbogenerator power output and constant generator shaft speed, decreasing the generator diameter would require additional generator length, while increasing the generator diameter would require a shear stress reduction.

The right-hand graph in Figure 2-14 describes a set of different turbine shaft powers for a single-stage, radial turbine (represented by solid lines). Assuming a turbine adiabatic efficiency of 30 %, a generator efficiency of 80 %, a power electronics efficiency of 90 %, a work coefficient of 1 and a flow coefficient of 0.3, the turbine design space is limited by three constraints at constant output: supply pressure ratio, blade manufacturability considerations, and smallest allowable turbine diameter.

Figure 2-15, analyzes in more detail the 50 W design space and the impact of different turbine manufacturing technologies, as well as the impact of different generator types. The turbine assumptions are consistent with high-fidelity simulation results presented in Chapter 3. The major observation is that in a narrowly constrained design space only a MEMS turbine near 500,000 rpm yields a viable 50 W, low flow turbogenerator design.
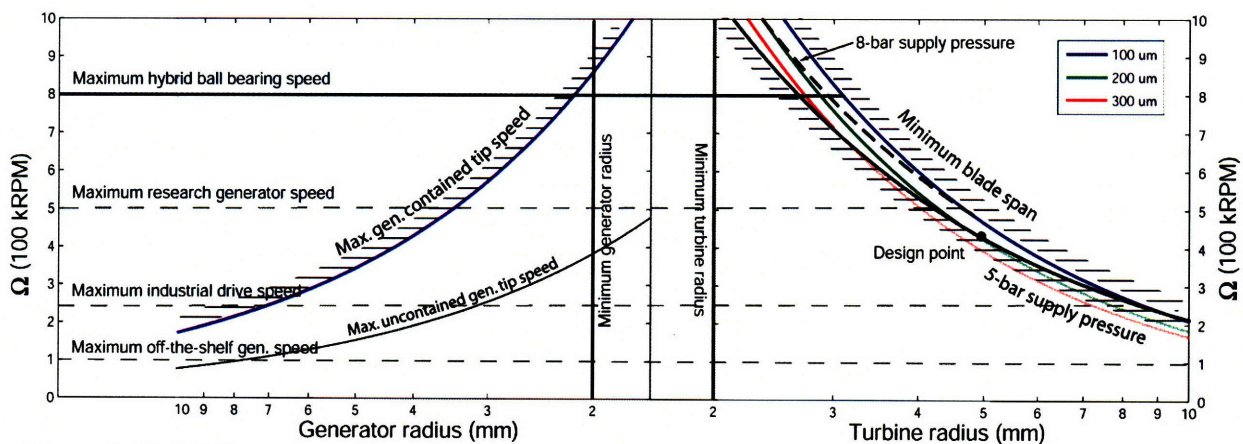

Figure 2-15: 50 W turbogenerator design space, illustrating the generator and turbine size, speed and tip speed constraints, and the hybrid ball bearing speed limit.

The left-hand plot in Figure 2-15 depicts the generator design space with and without the containment hoop constraint, derived from Equation (2-6) and Equation (2-7). Furthermore,

horizontal lines indicate current generator speed limits depending on the generator type. The maximum generator mechanical stress in combination with the minimum manufacturable generator rotor diameter alone does not justify the horizontal lines that limit the generator speeds: bearings, friction losses, tolerances and balancing are issues for these generators as well. Off-the-shelf generators operate well below the tip speed limit of a contained or uncontained generator rotor. Rather, as discussed qualitatively by Kafader in [16], they are limited due to achievable manufacturing tolerances and friction losses. In [16] it is argued that "miniaturization below 10 mm asks for new solutions concerning bearings, commutation systems and magnetic material. At the same time new manufacturing and mounting concepts are needed." These limitations are captured by the horizontal line at 100,000 rpm for off-the-shelf generators. Industrial drives have power outputs in the kW range and achieve maximum speeds of 250,000 rpm, based on a market survey reported by Kolar [19]. Qualitatively, these generators require high speeds. Thus, in order to surmount the tip speed constraint of an uncontained rotor, containment hoops are used. The allowable hoop stress in combination with achievable manufacturing tolerances limits the maximum speed of the industrial drives to 250,000 rpm. The horizontal line at 500,000 rpm represents the current maximum speed achieved by research generators, reported in [19]. These generators are constrained by losses resulting from high speed operation, the availability of bearings and achievable manufacturing tolerances. The required high manufacturing precision currently makes these design speeds only achievable by research projects. These generators require containment hoops and high speed bearings, such as hybrid ball bearings or air bearings. Further increasing generator speeds would require smaller generator radii, which in turn makes the rotors more difficult to manufacture, and gives rise to increased friction losses and stricter tolerances requirements. The feasibility of these generators has yet to be demonstrated.

The right-hand side of the graph illustrates the relation between rotor speed and turbine radius for a 50 W turbogenerator electric output assuming three different sets of blade spans, marked by the solid lines. Each blade span contour corresponds to the minimum feature size achievable by a certain manufacturing technology: the 300 um blade span corresponds to micro-milling, 200 um correspond to SDM, and 100 um correspond to DRIE. Note that DRIE can achieve smaller blade spans, but that efficiency considerations limit the minimum blade span to 100 um. The key message from the chart is that the viable turbine design space is

narrowly constrained by two limitations: the 5-bar pressure supply and the minimum allowable blade span. As turbine rotor diameter decreases and shaft speed increases, the viable turbine design space broadens and larger blade spans become feasible.

A turbine design with 200 um blade span, achievable only by unconventional manufacturing technology, becomes feasible near 500,000 rpm. This rotor speed is currently achieved by research generators, such as for example [37]. A conventional micro-milled 300 um blade span requires rotor speeds above 700,000 rpm, which demands a significant advance in generator technology. The research generator reported in [19] was operated up to a speed of 740,000 rpm without load, and experienced significant losses and possible rotor integrity challenges. Furthermore, the maximum speed of the hybrid ball bearings is assumed to be 800,000 rpm. At these speeds, air bearings become preferable because the lifetime of hybrid ball bearings is unknown and could cause reliability issues. Though the turbine design space is not constrained by the minimum turbine radius, a sensitivity analysis shows that a turbine radius of 3 mm would limit the maximum achievable rotor speed from 600,000 rpm to 800,000 rpm for a blade span of 300 um to 100 um respectively. Alternatively, operation at 8-bar would be possible for a 100 um blade span at 500,000 rpm and a turbine radius of 6 mm.

In conclusion, a turbine with 220 um blade span at 450,000 rpm is deemed a viable design configuration for low-flow, high pressure ratio operation with a targeted turbogenerator power output of 50 W. The relatively short blade span requires DRIE manufacturing technology. In summary, the proposed turbogenerator design combines a silicon based MEMS turbine with a meso-scale generator.

2.9. Conclusions

The preferred system architecture is a single-stage radial inflow turbine in combination with a permanent magnet, cylindrical-shaped generator. Scaling laws to assess the system power as a function of rotor diameter and shaft speed were established. The major constraints and design trade-offs were analyzed: manufacturing of the turbine blades, centrifugal stress in the generator, and low mass flow considerations. To comply with the low mass flow consumption requirement, the turbine must be designed for high specific work. Furthermore, the low mass flow yields turbine designs with relatively short blade spans, which introduces a

manufacturing challenge. To obviate this constraint and to increase turbine efficiency, an unconventional manufacturing technology for a high speed turbine design is required. Since the generator and turbine designs are integrated, the major trade-off is between high shaft speed of the turbine and structural integrity of the generator. To meet the low mass flow requirement and while relieving the manufacturing constraint, DRIE manufacturing technology is identified as a viable turbine fabrication option.

Chapter 3.   High Speed Turbine Design

3.1.   Design Point Selection and Proposed Design

The challenge is to design a 50 W, low flow turbogenerator operating at an air-supply pressure of 5 bar. In order to meet this challenge, the objective is to design a high specific-work, low flow, radial single-stage turbine that accommodates the generator and manufacturing constraints. A 100 W, 500,000 rpm generator has been operated successfully and is discussed in detail in [37]. This research generator currently yields the highest speed at the torque rating of interest. As discussed in the previous chapter, a turbine design speed of 450,000 rpm is chosen, compatible with the research generator described above. Nevertheless, the turbine design remains challenging, since the resulting turbine blade span of 200 um is below the conventional manufacturability limit of 300 um. Figure 3-1 illustrates the proposed design choice and conceptually outlines the trade-off between rotor speed and turbine blade span.
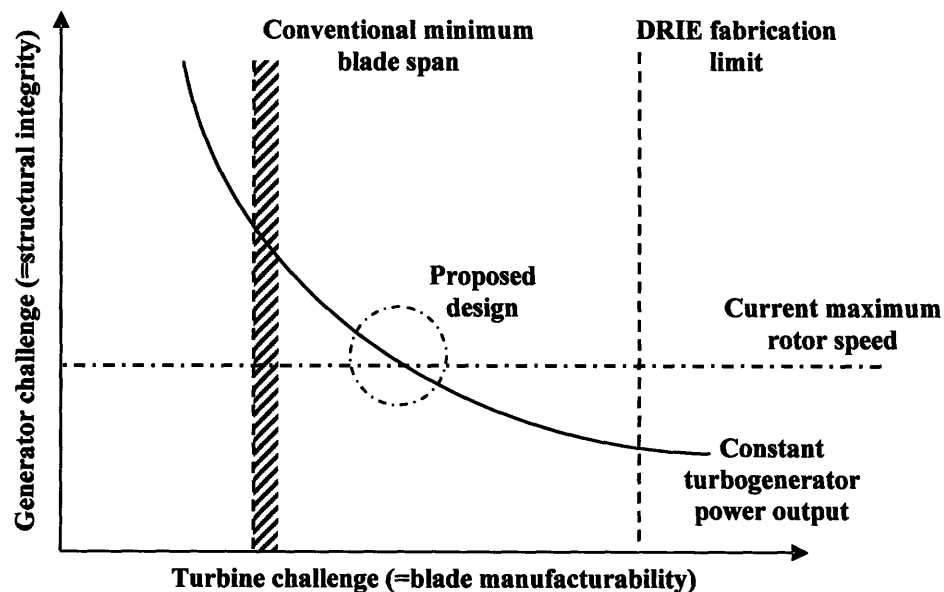
Figure 3-1: Design trade-off between rotor speed (generator structural integrity) and turbine blade span (manufacturability limit).

45

3.2. Design Methodology

The design approach begins with a thermodynamic analysis that sets the fundamental turbine parameters: rotor diameter and shaft speed. This analysis was carried out in Chapter 2. The combined effect of all loss mechanisms in the turbine is captured by an estimated turbine adiabatic efficiency. Then, employing a mean-line analysis, in which the stagnation pressure loss is modeled through loss coefficients, the velocity triangles and relevant pitch-wise averaged quantities are defined. Next, the turbine blade profiles are designed using MISES, a 2D coupled, viscous/inviscid Euler solver. Profile losses and shock losses are assessed. Finally, 3D Reynolds Averaged Navier-Stokes calculations of the entire turbine stage are conducted. The commercial code FLUENT is used for isolated stator and rotor flow simulations, capturing end-wall losses, profile losses, secondary flow losses and shock losses. Since end-wall losses are dominant due to the relatively low blade aspect ratios of 0.2, it is crucial to carry out 3D simulations. Figure 3-2 summarizes the different steps in the design methodology.
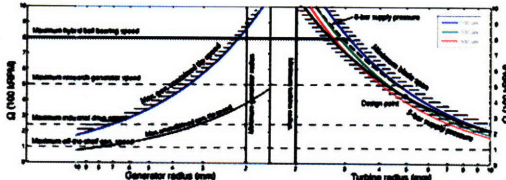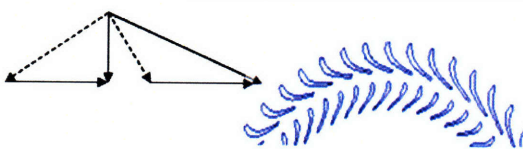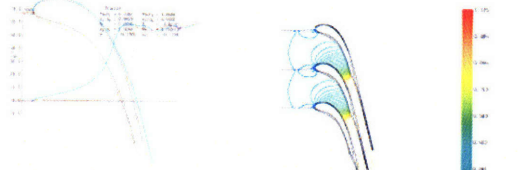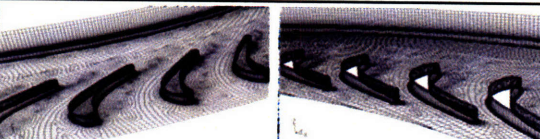
Steps	Outcome	
0D: Thermodynamic analysis	• Turbine rotor diameter • Rotor shaft speed	
1D: Mean line analysis	• Velocity triangles • Pitch wise averaged mean flow	
2D: Blade profile design and optimization	• 2-D flow field • Camber line • Thickness distribution • Solidity • Profile losses	
3D: Three dimensional RANS simulations	• Endwall loss effects • 3-D flow field	

Figure 3-2: Design methodology.

3.3.   Mean-Line Analysis

The mean-line analysis determines the pitch-wise averaged flow field, based on a procedure described in [17] and [26]. The total pressure and total temperature are specified at the turbine stage inlet, along with the stage geometry (shaft speed, NGV trailing edge angle, NGV outlet radius, rotor inlet and outlet radius, and blade span). The method computes the mass flow and determines the resulting exit static pressure and shaft work. The approach is iterative and, when the exit static pressure matches ambient pressure, the analysis is deemed converged. The method outputs total and static pressures, temperatures and velocities at the NGV inlet and outlet, rotor inlet and outlet, and stage exit. Furthermore, it estimates the adiabatic turbine efficiency. Figure 3-3 illustrates the flow diagram of the mean-line method.

```
            ┌─────────────────────────────────┐
            │      Set flow conditions         │
            └─────────────────────────────────┘
                            │
            ┌─────────────────────────────────┐
            │      Set stage geometry          │
            └─────────────────────────────────┘
                            │
            ┌─────────────────────────────────┐
        ┌──▶│      Assume mass flow            │
        │   └─────────────────────────────────┘
        │                   │
        │   ┌─────────────────────────────────┐
        │   │      Estimate NGV losses         │
        │   └─────────────────────────────────┘
        │                   │
        │   ┌─────────────────────────────────┐
        │   │      Estimate rotor losses       │
        │   └─────────────────────────────────┘
        │                   │
    NO  │   ┌─────────────────────────────────┐
        │   │    Determine velocity triangles  │
        │   └─────────────────────────────────┘
        │                   │
        │   ┌─────────────────────────────────┐
        │   │      Estimate exit turn losses   │
        │   └─────────────────────────────────┘
        │                   │
        │   ┌─────────────────────────────────────┐
        └───│ Exit static pressure = ambient pressure? │
            └─────────────────────────────────────┘
                            │ YES
            ┌─────────────────────────────────┐
            │      Stage performance           │
            └─────────────────────────────────┘
```
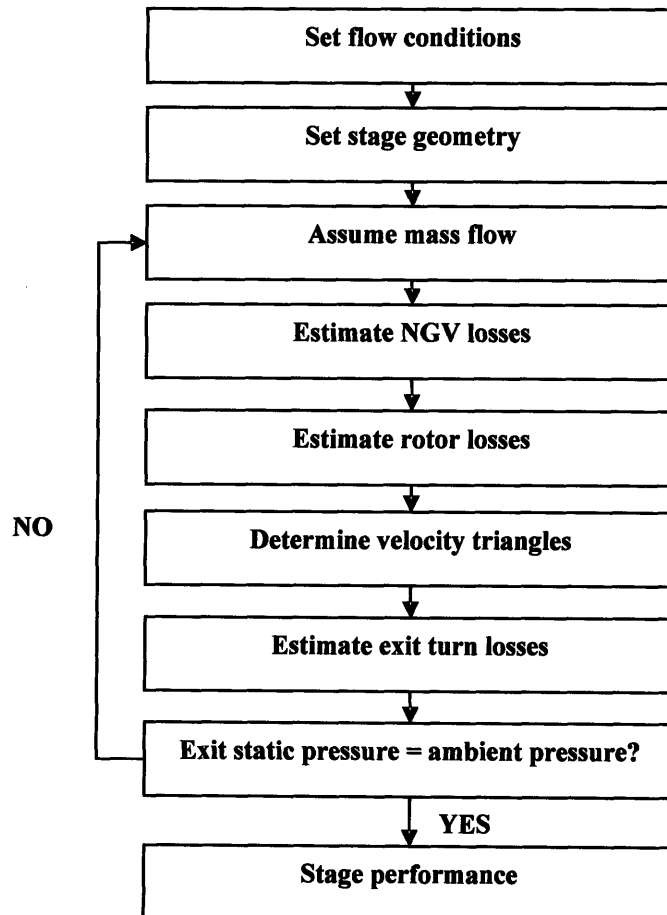
Figure 3-3: Flow diagram of mean line method.

Table 3-1 summarizes the stage characteristics for the candidate design discussed in Chapter 2. Table 3-2 depicts the non-dimensional stage characteristics. Based on these results, the velocity triangles are drawn in Figure 3-4.

Table 3-1: Summary of high speed turbine design.

NGV inlet radius	6.3 mm	Rotor blade span	200 um
NGV outlet radius	5.3 mm	Rotor tip clearance	20 um
NGV leading edge angle	-5°	Inlet total pressure	5 bar
NGV trailing edge angle	78°	Inlet total temperature	300 K
Rotor inlet radius	5.0 mm	Outlet static pressure	1.013 bar
Rotor outlet radius	4.0 mm	Outlet total temperature	250 K
Rotor leading edge angle	45°	Rotor rotational speed	450,000 rpm
Rotor trailing edge angle	-55°	Shaft power	77 W
Mass flow	1.45 g/s	Device efficiency	48 %

Table 3-2: Summary of non-dimensional turbine stage characteristics.

M_{tip}	M_{exit}	ϕ	Ψ	σ
0.75	0.50	0.30	0.97	0.18

Station 1: rotor outlet   Station 1: NGV exit (rotor inlet)
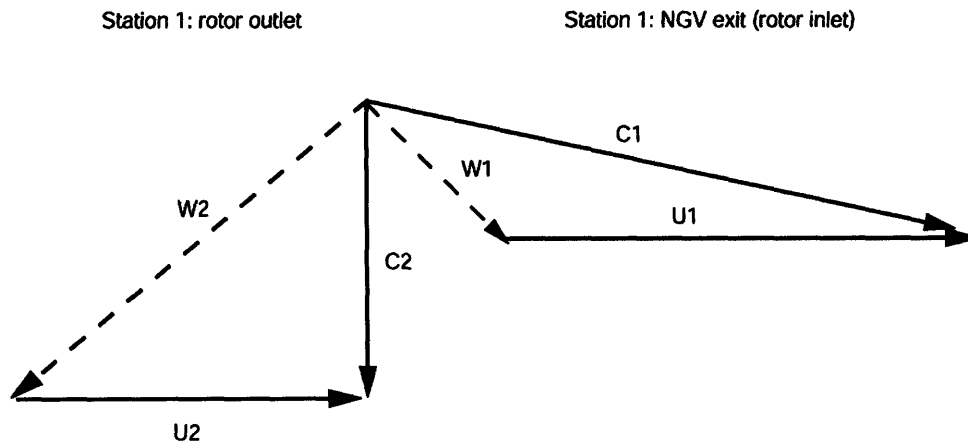

Figure 3-4: Velocity triangles of high speed turbine design.

3.4.   *Turbine Blade Profile Design*

Once the required flow angles are determined from the mean-line analysis, the blade profiles need to be designed. The camber line, the blade thickness distribution, the blade chord, c, and the blade pitch, s, are determined. The blade aspect ratio, $\frac{h}{c}$, and solidity, $\frac{c}{s}$, are then defined. The procedure is repeated until a suitable blade loading distribution is found. The number of rotor and stator blades is chosen such that the required flow turning is achieved while keeping profile losses and trailing edge flow deviation as low as possible.

3.4.1. Stator Blade (NGV) Design

Conventional stator blades in turbochargers can be simple wedges and uncambered, as shown in Figure 3-5. A cambered design, illustrated in Figure 3-6, is similar to axial turbine nozzle designs. Leading edge camber reduces overspeed on the suction side and helps turning the flow. Since the blade profile losses scale with Mach number cubed, it is desirable to avoid high Mach numbers over the suction side. Figure 3-7 depicts the resulting camber line as dotted line in the blade profile.

Figure 3-5: Wedge stator blade design [30].

Figure 3-6: Cambered stator blade design [30].

The blade thickness distribution is determined using MISES [6], a finite volume Euler code coupled to the integral boundary layer formulations (IBLT). A key feature of MISES is

that it allows inverse design, i.e., blade profiles can be found based on specified pressure coefficient distributions,

$$C_p = \frac{p - p_1}{\frac{1}{2} \cdot \rho \cdot V_1^2}. \tag{3-1}$$

This feature is used to avoid any local Cp spikes on the blade surface which can lead to increased profile losses. Figure 3-7 shows the acceleration along the stator blade. The flow is choked at the throat, as indicated by the horizontal dotted line in Figure 3-7. The stator blade is designed for zero incidence at design conditions. The blade geometry definition is non-dimensional, i.e. the thickness distribution is defined in percent chord, $\frac{t}{c}$.
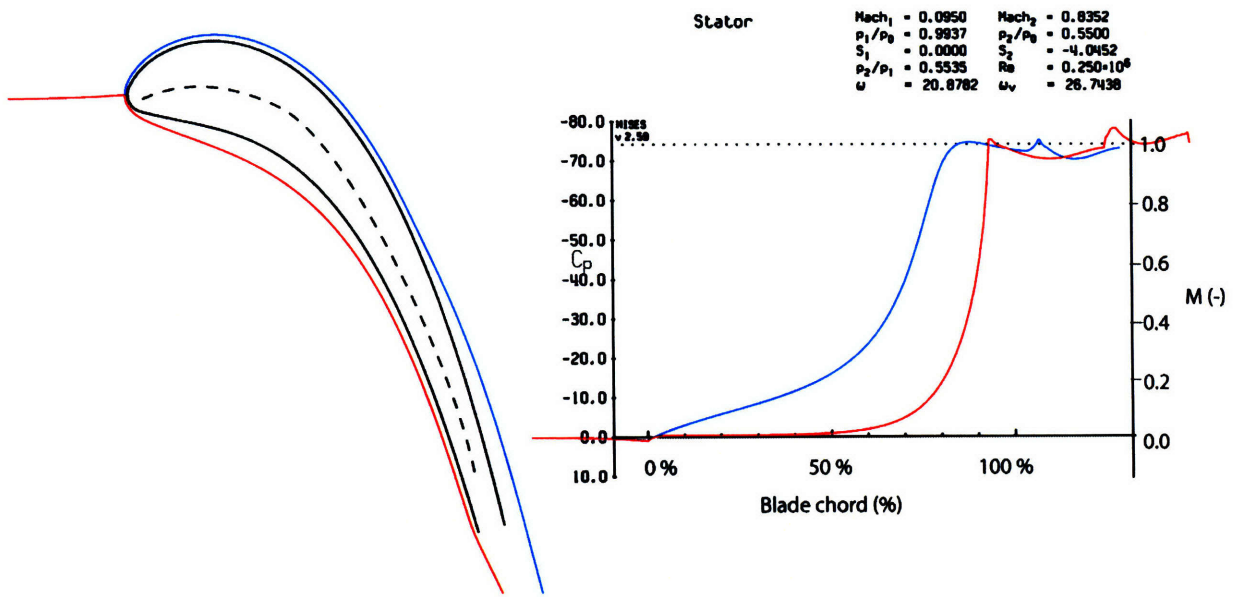

Figure 3-7: Cp profile of stator blade.

Next, the blade aspect ratio is determined based on the blade span, previously found by the mean-line analysis. Since end-wall losses dominate over profile losses due to the low aspect ratio, a minimum wetted surface is desirable, equivalent to shorter blade chord for a given blade span. Experience from the MIT Micro-Engine Project shows that a blade aspect ratio of about 0.2 is required to avoid blade root stress problems in the brittle silicon material [14]. Hence, a blade span of 200 um yields a blade chord of 1 mm.

The solidity can be determined using empirical correlations (e.g. the Zweifel loading coefficient [17]) or blade-to-blade calculations in MISES. Figure 3-8 shows MISES results for different blade solidities. The loss coefficient is defined as total pressure loss over the exit dynamic head

$$\omega = \frac{p_{t,1} - p_{t,2}}{p_{t,2} - p_{s,2}},$$ (3-2)

and the deviation angle δ is defined as

$$\delta = \alpha_{design} - \alpha_{MISES}.$$ (3-3)

A stator solidity of 2 is chosen, which is equivalent to 40 blades. This choice results in an acceptable flow deviation, while keeping profile losses low. The resulting stator blade row is depicted in Figure 3-9.
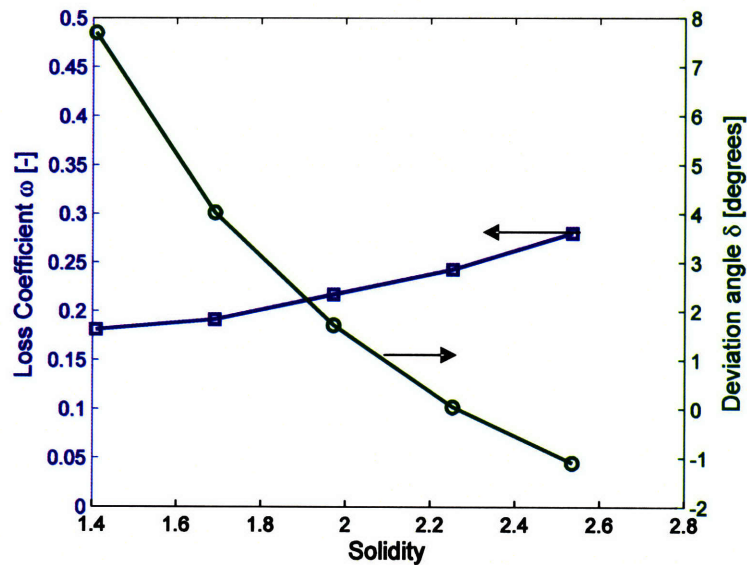

Figure 3-8: Loss coefficient and deviation angle as function of stator solidity.
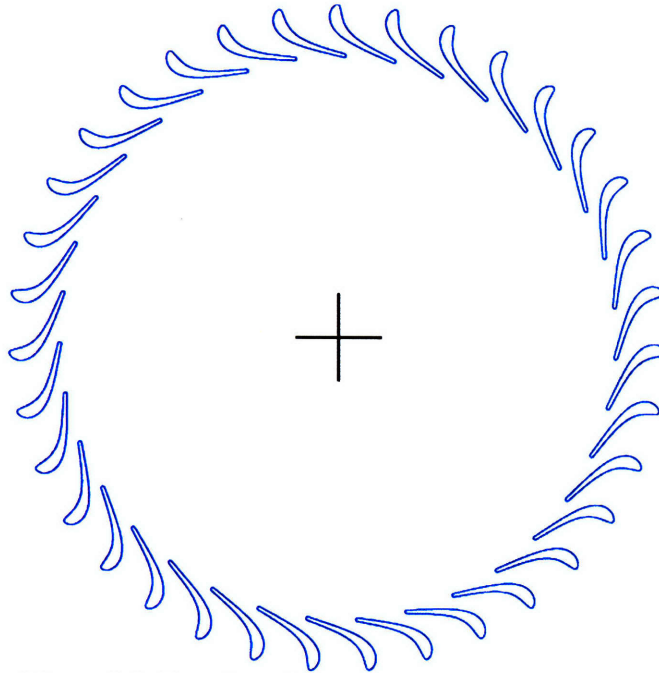
51

N = 40
h/c = 0.2
c/s = 2.0

Figure 3-9: Top view of stator blade row.

3.4.2. Rotor Blade Design

The rotor blade row is designed using the same approach. Figure 3-10 shows the rotor blades. Note that the blade leading edge angle is not radial and back-swept by -45°. This allows for an increased work coefficient while meeting the blade stress limits of silicon with a sufficient margin.
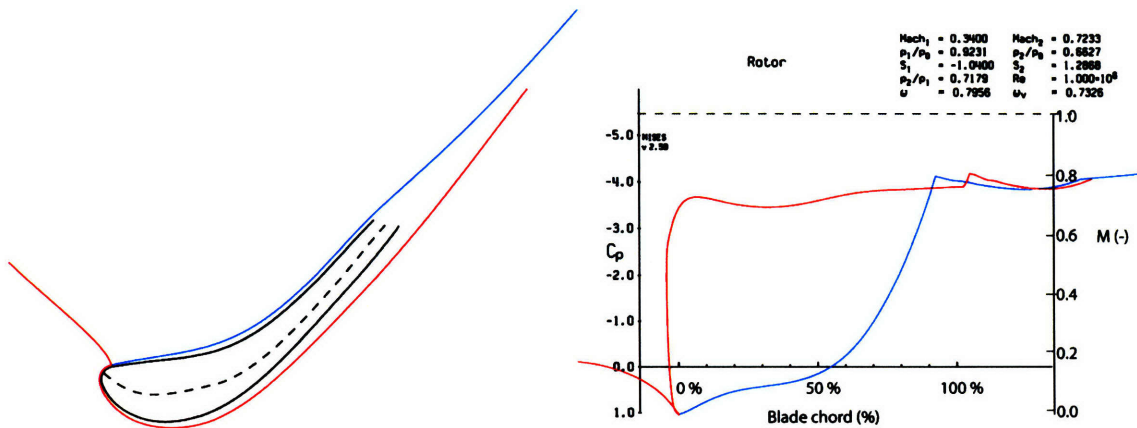

Figure 3-10: Cp profile of rotor blade row.

The thickness distribution is determined as for the stator design, and Figure 3-10 depicts the resulting Cp profile. The relatively low Cp values in comparison to the NGV indicate a flow that is turned rather than accelerated, typical of low reaction turbines. Furthermore, the Mach number is kept below sonic conditions, as indicated by the horizontal dotted line in Figure 3-10. The flow chokes in the stator, setting the mass flow through the turbine stage.

Similar to the NGV, stress considerations limit the rotor chord to blade span ratio and the rotor blade chord is set to 1 mm. For various rotor blade solidities, the rotor loss coefficient[3] and deviation angle are again determined using MISES. Based on the results shown in Figure 3-11, a solidity of 2.4 is chosen, yielding 35 rotor blades. Figure 3-12 depicts the resulting rotor blade row.
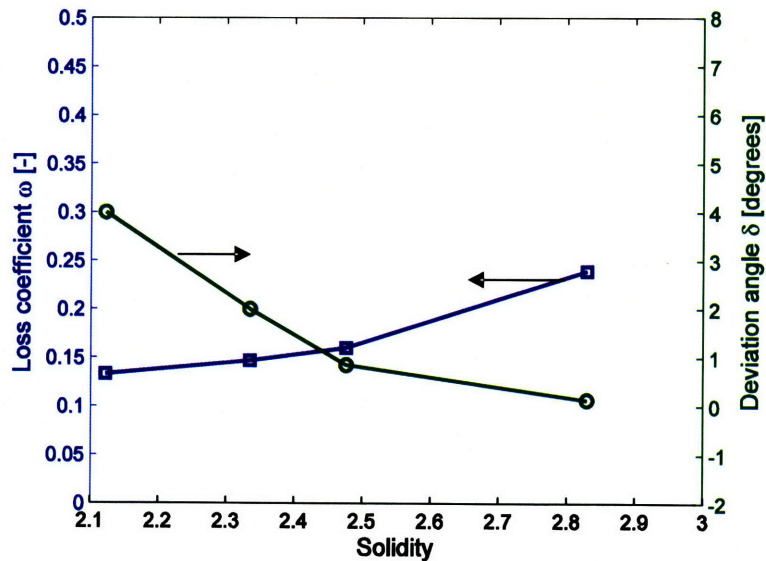

Figure 3-11: Loss coefficient and deviation angle versus rotor solidity.

---

[3] The rotor loss coefficient is defined using the relative stagnation pressure.
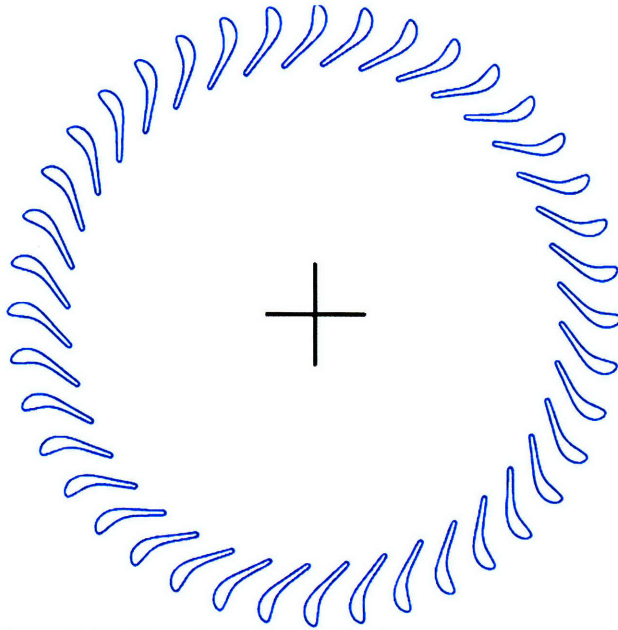
N = 35
h/c = 0.2
c/s = 2.4

Figure 3-12: Top view of rotor blade row.

3.4.3. Turbine Stage Design

Figure 3-14 shows a top view of the complete turbine stage. A critical dimension is the choice of stator-rotor radial spacing. Figure 3-13 illustrates Cp contours of the rotor flow field. To avoid aerodynamic forcing and potential stator blade fatigue due to the upstream influence of the rotor blades, the rotor-stator spacing has to be chosen carefully. At a radial distance of about 1/3 of the rotor chord, the non-uniformity of the pressure field has significantly decayed such that the stator-rotor spacing is set to 0.3 mm.

In summary, the stator has 35 blades, the rotor 40 has blades. The stage is designed for a mass flow of 1.45 g/s and a total-to-static pressure ratio of 5 at 450,000 rpm.

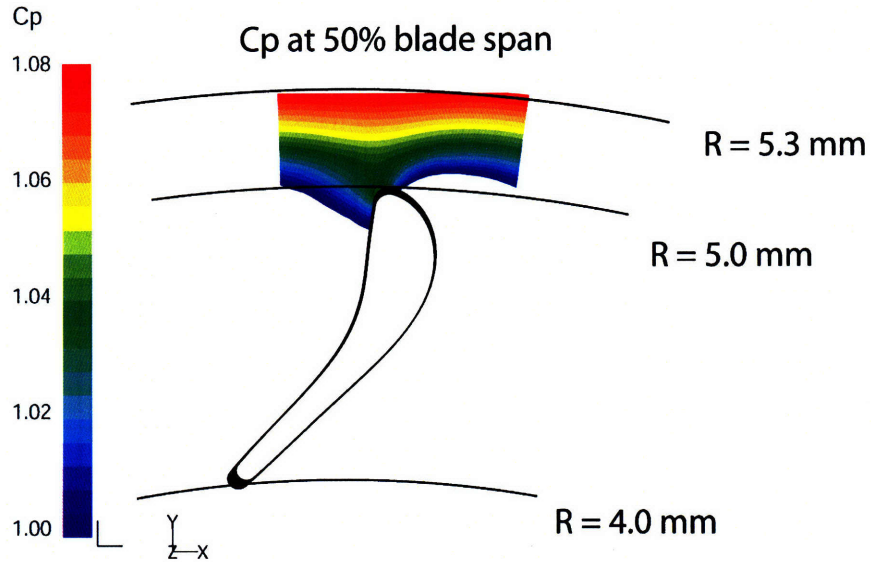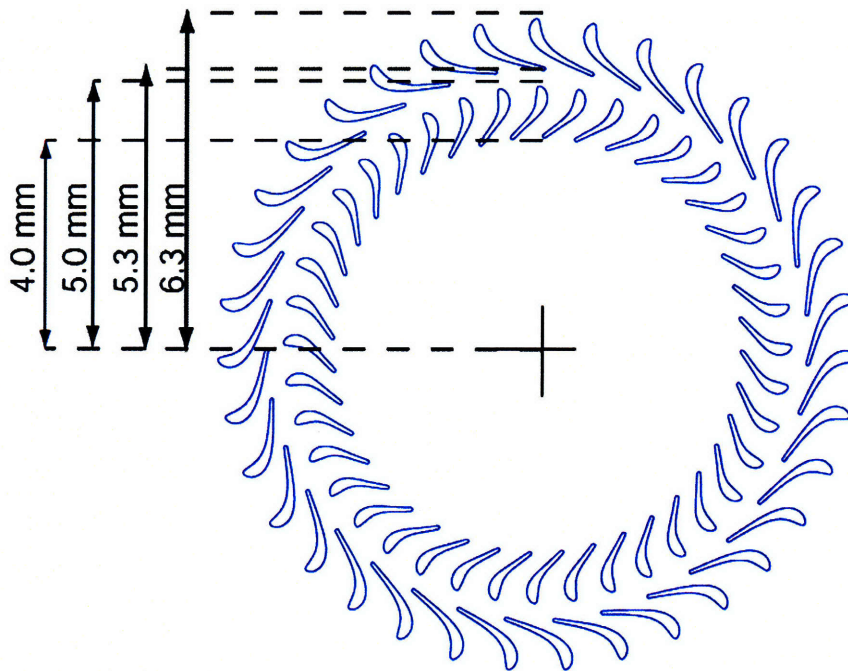**Figure 3-13: Contours of pressure coefficient at 50% blade span.**

Figure 3-14: Top view of high speed turbine stage.

3.5. 3D Steady RANS Analysis

The objective is to assess the turbine performance at design conditions using high-fidelity 3D simulations. Since 3D losses dominate the profile losses, a full 3D simulation is required to investigate the turbine performance. There are two dominant loss sources that

require attention: end-wall losses that result from the low blade aspect-ratio and tip leakage losses that result from the relatively large tip clearance gap to blade span ratio.

3.5.1. Computational Domain and Passage Interface
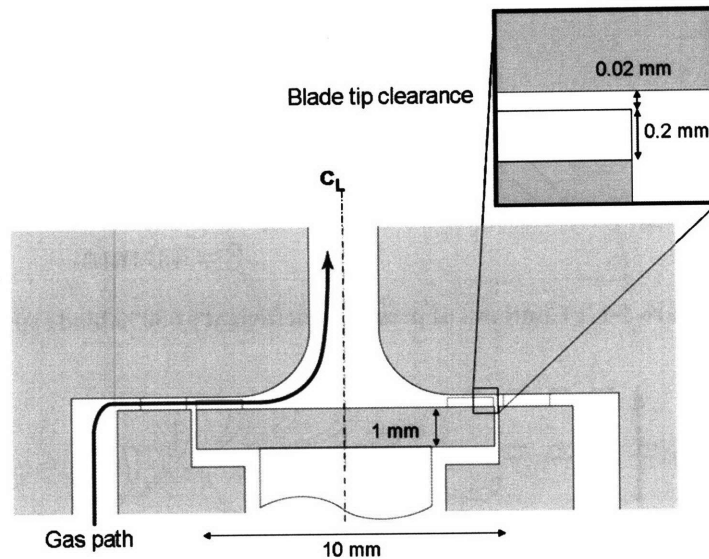
Figure 3-15: Gas path geometry of the turbine stage.

Figure 3-15 illustrates the gas path geometry of the turbine stage. Two separate computational domains are used for the simulation of the turbine stage, one for the stator and one for the rotor. Figure 3-16 illustrates the stator grid and the rotor grid separated by an interface. The stator grid has 225,000 cells, while the rotor grid has 190,000 cells. The rotor tip gap grid has 20,000 cells. A grid sensitivity analysis was conducted and the results show that this grid density is sufficient to resolve the key flow features of interest. More details can be found in Appendix A.

Figure 3-16: Computational domain definition.

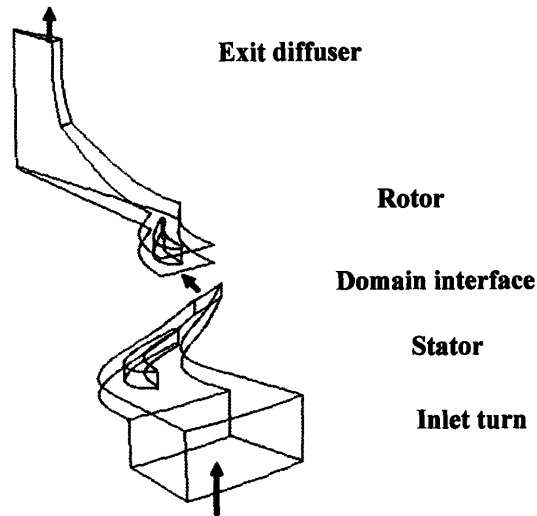Since the stator and the rotor simulations are run as two separate computations, the two flow fields have to be linked through an interface. It is assumed that unsteady phenomena such as blade-wake interaction can be ignored. The following conditions are used at the domain interface.

Mass flow matching: The mass flow through the NGV is equal to the mass flow through the rotor.

Stagnation temperature matching: The mass averaged stagnation temperature at the NGV domain exit is used as the inlet stagnation temperature to the rotor.

Stagnation pressure matching: The mass averaged stagnation pressure at the NGV domain exit is used as the inlet stagnation pressure to the rotor. For adiabatic flow, the mass averaged relative stagnation pressure at a given location represents the entropy flux at that station.

3.5.2. Numerical Mesh

3D grids were meshed with the commercial software GAMBIT. The grids around the blades are obtained by extruding a 2D grid. The passage in the rotor is split into two domains: a bottom domain 200 um thick that contains the blade and an additional domain 20 um thick that represents the tip clearance gap. The tip clearance grid is meshed with 20 cells and includes a boundary layer sub-grid for the leakage flow in the tip clearance. The stator and rotor inlet

domains are extended to allow viscous boundary layers to develop before the flow enters the blade row. The rotor grid is illustrated in Figure 3-17, and the stator grid is illustrated in Figure 3-18.
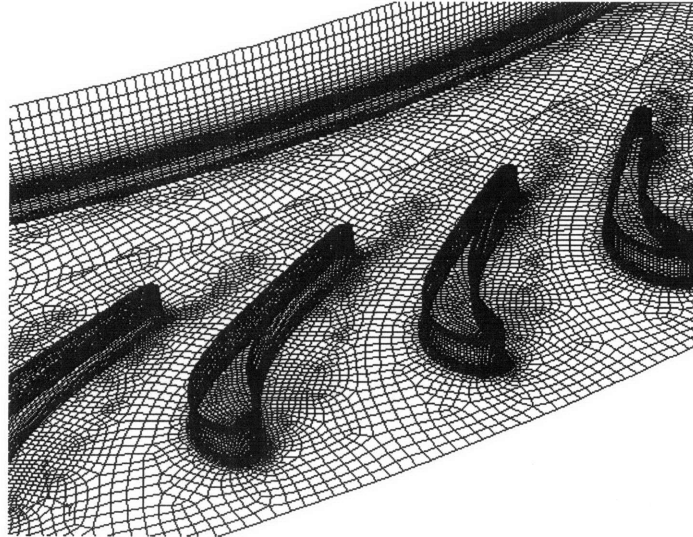
Figure 3-17: 3D view of rotor grid (not all cells shown).
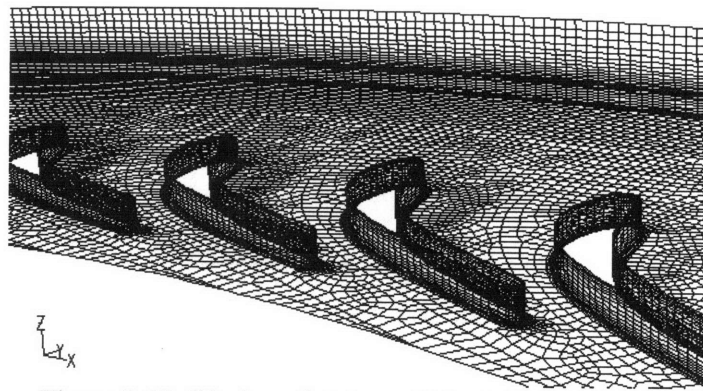
Figure 3-18: 3D view of stator grid (not all cells shown).

The areas upstream and downstream of the blade rows have a structured grid, while an unstructured grid near the blade is used. The mesh used for both 2D grids around the blade is of O-type topology with a boundary layer sub-grid, illustrated in Figure 3-19. The thickness of the boundary layer mesh is based on 2D MISES results; the boundary layer mesh along the blade is eight cells thick with an expansion factor of 1.3 yielding a y^+ value of 3. This yields a relatively high boundary layer density as y^+ is usually between 10 and 100 [10]. Furthermore,

the O topology yields adequate refinement close to the blade leading and trailing edges, and prevents numerical difficulties.
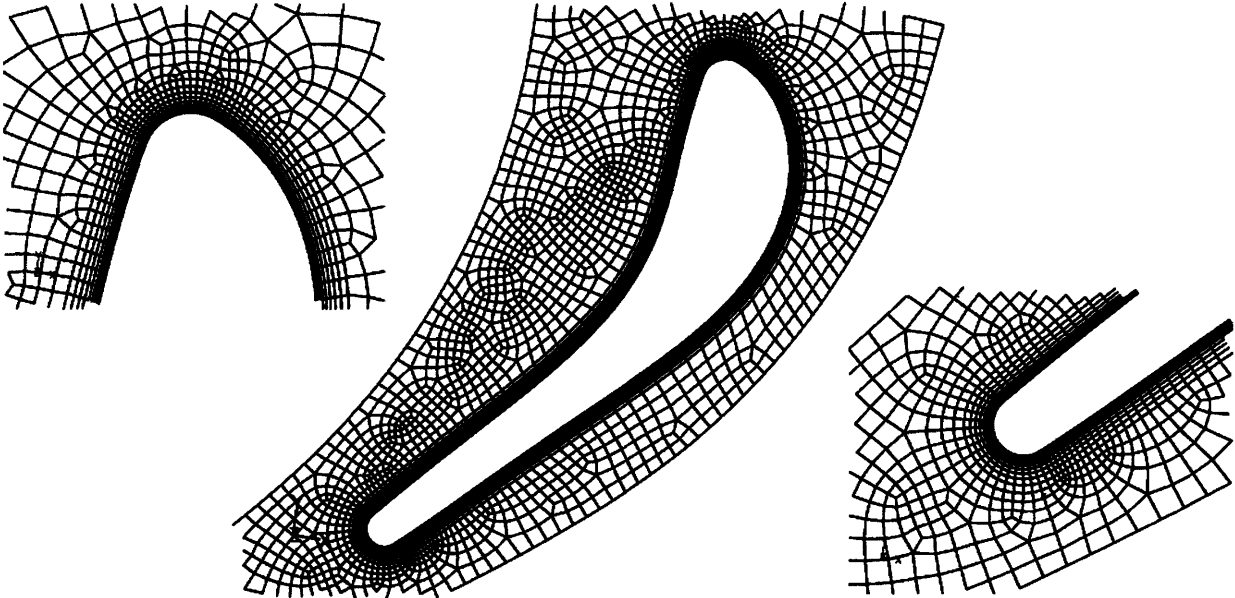
Figure 3-19: Top view of stator grid with O topology, including close up of the leading and trailing edge grid.

3.5.3. Diffuser Design

The flow out of the radial turbine needs to leave in the axial direction such that a 90° exit turn is required. This results in additional total pressure loss. The purpose of an upstream diffuser is to reduce the kinetic energy in the exit flow before it is turned in the axial direction. This lost work can be recovered as useful work, which increases the device efficiency. A straight channel diffuser is used to diffuse the flow, as illustrated in Figure 3-20.

Figure 3-20: Nomenclature of straight channel diffuser.

Design guidelines and design charts for straight channel diffusers can be found in [11]. A non-dimensional length $\frac{N}{W_1}$ of 9 and an effective area ratio $\frac{W_2}{W_1}$ of 2 are chosen. This ensures that the diffuser operates away from the appreciable stall and large transitory stall region, while maximizing the pressure rise coefficient. To diffuse the radially inward flowing turb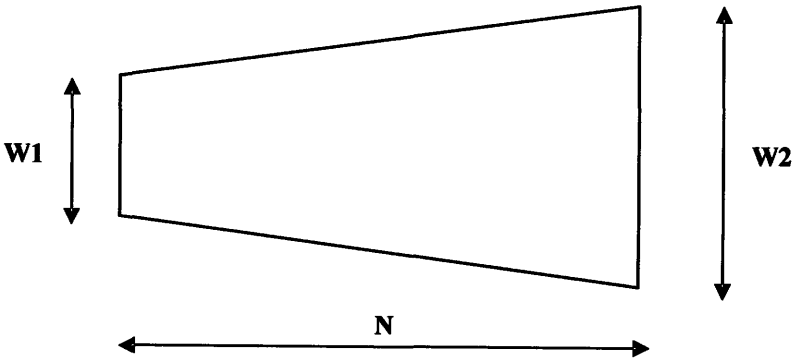ine exhaust air, the diffuser passage height needs to be adjusted accordingly. The resulting passage height varies quadratically with radius. Figure 3-21 shows the effective flow area and the passage height as a function of radius. The diffuser inlet is located at a radius of 3.8 mm, about a quarter chord downstream of the rotor blade row. The chosen non-dimensional length yields an effective diffuser length of 2 mm, such that the diffuser exit plane is at a radius of 1.8 mm, with an exit passage height of 0.92 mm.
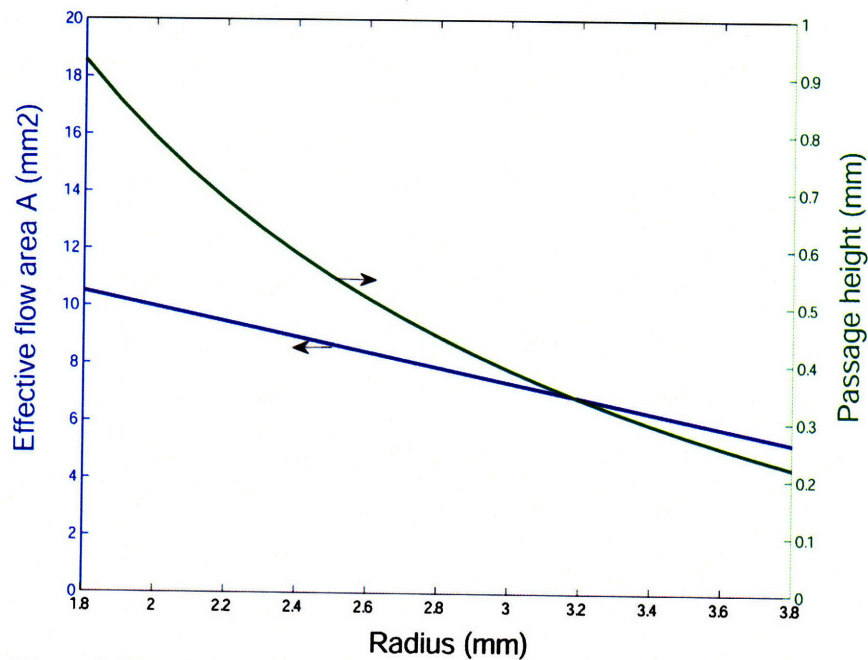

Figure 3-21: Effective diffuser flow area and passage height versus radius.

3.5.4. Convergence Criteria

The pressure-based, steady implicit solver is chosen using the second-order formulation, and the $\kappa - \varepsilon$ turbulence model. The high-order solution scheme coupled with the high grid

60

density guarantees the desired high fidelity. Convergence criteria are met when the residuals fall below 1e-5, and the stage mass flow becomes steady.

3.5.5. Turbine Performance Analysis

In order to assess the performance of the turbine, the lost work in the stage is analyzed. The amount of entropy generated in the turbine stage is determined based on the total temperatures and total pressures evaluated at various locations. The lost work can then be computed as

$$w_{lost} = T_0 \cdot \Delta s, \qquad (3\text{-}4)$$

where T_0 is the stage exit temperature. Figure 3-22 shows the stations at which the losses were calculated. The shaft power and the lost work are normalized by the ideal work, and shown in terms of a pie chart in Figure 3-23. The pie chart is useful for identifying major loss sources and in prioritizing areas for improvement.
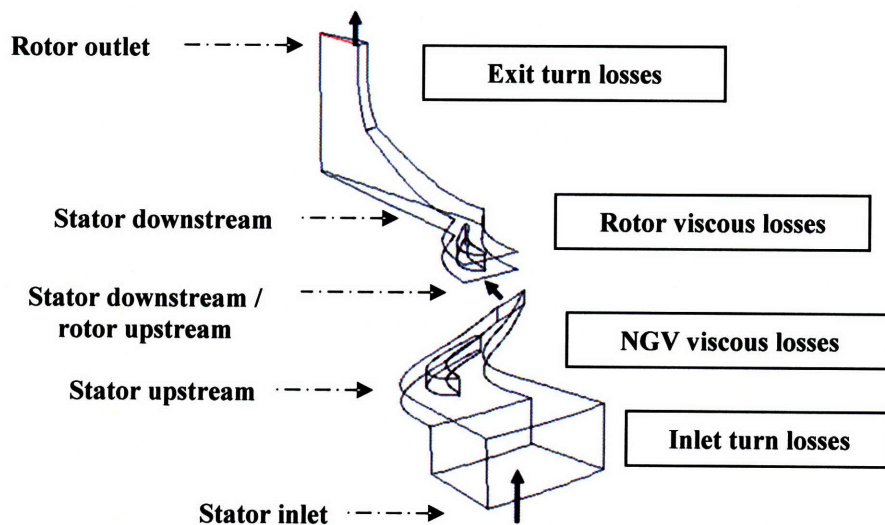

Figure 3-22: Overview of locations used for performance and loss analysis.
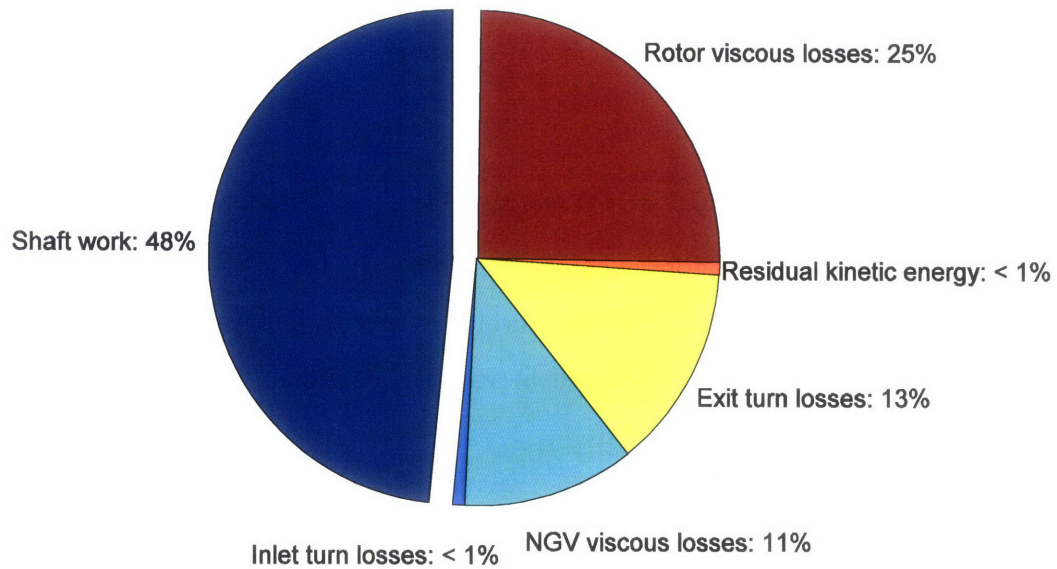
Figure 3-23: Loss break-down of turbine stage.

Figure 3-23 shows that the turbine output is only 48 % of the ideal work, due to viscous losses in the rotor, stator, exit turn and residual kinetic energy. The major loss source (25 %) is the rotor viscous loss. To illustrate the key mechanisms, the dimensionless profile loss coefficient can be approximated as

$$\frac{\Delta p_t}{\frac{1}{2}\rho U^2} = C_d \cdot \left(\frac{2\bar{u}}{\Delta u} + 6\frac{\Delta u}{\bar{u}} \right)(\tan\alpha_2 - \tan\alpha_1), \qquad (3\text{-}5)$$

where C_d is the dissipation coefficient, which depends on the Reynolds number, the mean velocity along the turbine blade $\bar{u}$, the difference between the high velocity on the suction surface and the low velocity on the pressure surface Δu, and the flow turning between the leading and trailing edge $(\tan\alpha_2 - \tan\alpha_1)$ [11]. There are three effects responsible for the rotor profile losses: high flow turning (more than 90°), the low Reynolds number and the high mean velocity. The high flow turning is directly related to the high work coefficient and the low Reynolds number is due to the small device scale. In addition to the profile loss, tip leakage loss and end-wall losses further deteriorate the turbine performance. The effect of the tip clearance on adiabatic turbine efficiency can be estimated using correlation results from [29]

Impulse turbine $(\sigma = 0)$: $\qquad \dfrac{\eta_{tip,clearance}}{\eta_{Design}} = 1 - 1.58 \cdot f$

Reaction turbine $(\sigma = 0.5)$: $\qquad \dfrac{\eta_{tip,clearance}}{\eta_{Design}} = 1 - 2.75 \cdot f$

$\qquad\qquad\qquad\qquad\qquad\qquad\qquad\qquad\qquad\qquad\qquad\qquad$ (3-6)

where f is the tip clearance to blade span ratio. Hence, for a 200 um blade span and a 20 um tip clearance, lost work due to the tip clearance losses is about 9% of the ideal work for an impulse turbine and about 17 % for a reaction turbine. For a stage reaction of $\sigma = 0.18$, the lost work due to tip leakage effects amounts to 12 % of the ideal work. This estimate is illustrated in Figure 3-24.
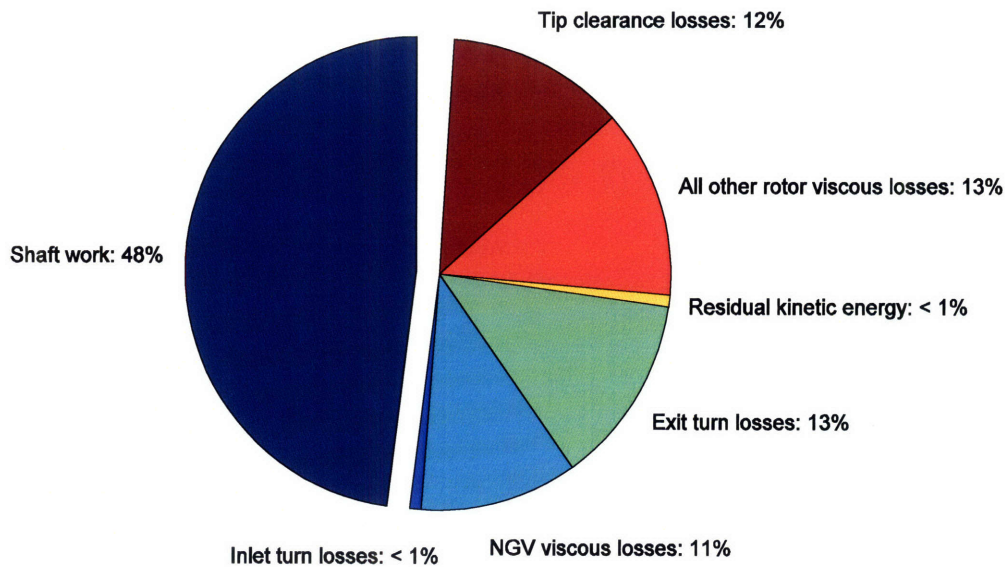
Figure 3-24: Turbine performance analysis including estimate of tip clearance losses.

The stator lost work represent 11 % of the ideal work and are mainly due to the high end-wall losses that stem from the low passage aspect ratio of 0.2, in contrast to typical passage aspect ratios of 1 – 2 for large scale turbines. The amount of stator viscous losses is similar to the remaining rotor losses. Lost work due to exit turn losses amount to 13 % of the ideal work. The lost work due to inlet turn losses and the residual kinetic energy account for less than 1 % of the ideal work and are negligible. There is a significant difference between the losses predicted by MISES and the losses predicted by FLUENT. This is due to the end-wall losses that can not be captured by 2D MISES computations, making a full 3D assessment is necessary.

3.5.5.1. Inlet Turn Losses

The device architecture requires 90 degree flow turns which must be designed carefully to reduce associated losses. This is achieved by reducing the flow Mach number through the turns. As illustrated in Figure 3-23, the inlet turn losses represent less than 1 % of the available work. The inlet turn losses are low for two reasons: first, there is a favorable pressure gradient due to the flow acceleration, which thins the boundary layer and reduces blockage; second, even if the flow separates at the sharp corner, it reattaches quickly after the turn, as illustrated in Figure 3-25. A separation bubble with reversed flow is visible just downstream of the 90° inlet turn.

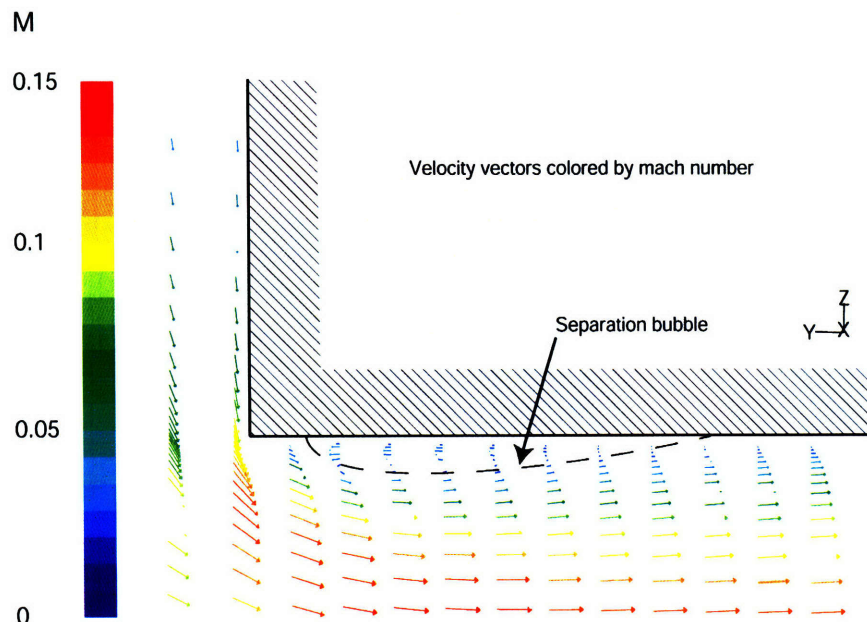**Figure 3-25: Velocity vectors colored by Mach number illustrating flow in inlet turn, with indication of a separation bubble.**

3.5.5.2. Diffuser performance

The main purpose of the diffuser is to reduce the Mach number and thus dynamic pressure before the flow undergoes a 90° turn. Figure 3-26 shows Mach number contours of the diffuser flow, with the flow entering at a radius of 3.8 mm. The flow Mach number is

reduced from 0.8 to 0.4, while the boundary layers remain attached. As a result, the Mach number at the turn is much reduced, mitigating the associated total pressure losses.
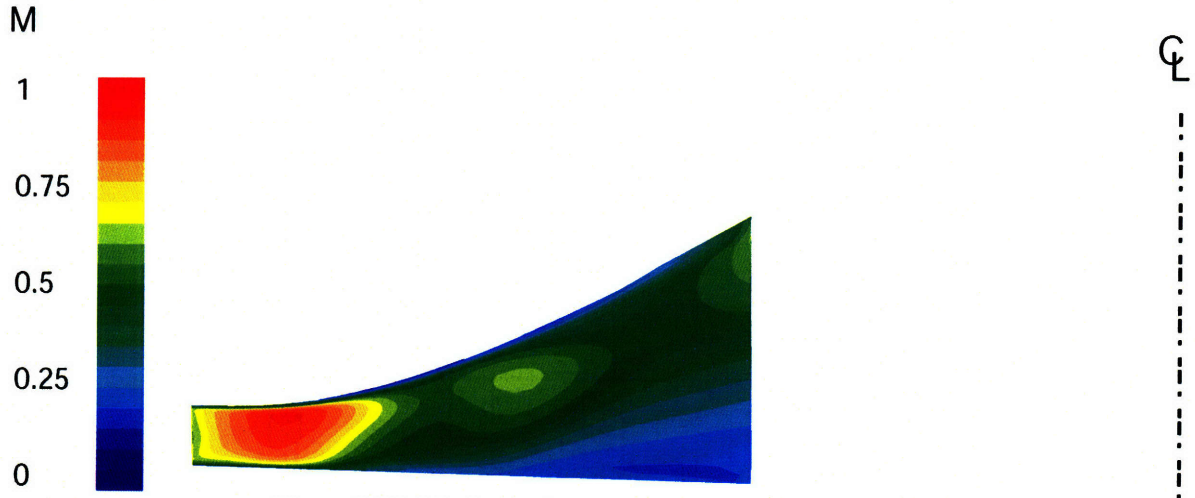
Figure 3-26: Mach number contours of the diffuser flow.

3.6. *Proposed 50 W Turbogenerator System*

Figure 3-27 depicts the proposed turbogenerator design using the generator geometry described in [37]. There are several points to note about the proposed design.

Rotor dynamics: The rotor dynamics of the generator shaft system are not altered due to the overhung silicon turbine disc. As described in [37], the generator operates at 500 krpm between the second and third bending mode.

Start up: The start-up of the turbine is not expected to be problematic, due to the low reaction design of the turbine.

Housing: The housing dimensions are compact; the preliminary design indicates a length of 5 cm and a diameter of 2 cm. This is primarily due to the high speed design, dramatically reducing the size of the device.

Rotor displacement: The control of the blade tip clearance is of critical importance because turbine adiabatic efficiency strongly depends on the tip clearance gap. To further reduce the axial play of the rotor, a thrust bearing should be used.

Generator cooling: The air flow is routed around the stator core. Posts are used to connect the housing and generator stator core. The advantage of this configuration is that the

air flow cools the generator, and recuperates the Ohmic losses of the generator. This increases the power output of the turbine and the generator efficiency.
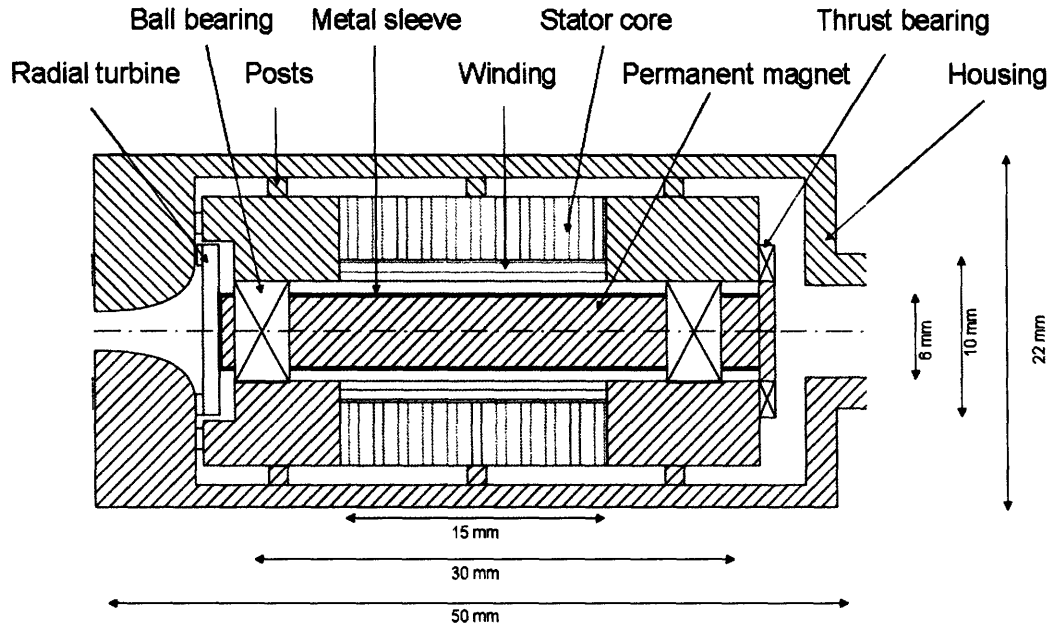
Figure 3-27: Turbogenerator assembly drawing.

3.7.   Conclusions

A high-fidelity, steady 3D CFD simulation was carried out to assess the turbine stage performance for 50 W net turbogenerator power output at a design mass flow of 1.45 g/s and a turbine total-to-static pressure ratio of 5. Table 3-3 summarizes the characteristics of the proposed design and compares it with other concepts found in the literature. The low flow, 50 W turbogenerator design is enabled by combining silicon chip manufacturing technology for the turbine with an existing high-speed research generator.

Table 3-3: Comparison of MIT turbogenerator designs with turbogenerator units found in literature.

	P_{shaft} (W)	m (g/s)	π (-)	Ω (rpm)	η_{ad} (%)
KUL [9]	20	4.0	1.8	150,000	18
MIT low speed design	77	4.0	5.0	150,000	20
MIT high speed design	77	1.45	5.0	450,000	48
ETH [8]	250	4.1	3	500,000	70

Chapter 4.   Conclusions   and   Recommendations   for Future Work

4.1.   Summary

This thesis presents the analysis, design and simulation of a turbogenerator for 50 W net electrical power output. A 5 bar air supply is assumed, and the turbogenerator is designed to draw a low mass flow from this supply because mass flow is considered a precious resource. Section 1.2.2 begins with a review of turbines and turbogenerators producing electrical power in the 1 W to 100 W range to identify the common themes dominating their designs. Based on these findings, the challenges for the design of a low-flow 50 W turbogenerator are formulated in Section 1.3. Section 2.1 presents the layout of the proposed turbogenerator system, designed to address the challenges. A detailed discussion of the low flow requirement follows in Section 2.2, which carries out a thermodynamic analysis to determine the required mass flow and to assess the impact of the desired low mass flow on the turbine design. Subsequently, the high-level design of the low-flow 50 W turbogenerator is developed through a four-step process. First, the system architecture is discussed in Section 2.5, and a single-stage radial inflow turbine and a permanent-magnet synchronous generator are chosen. Second, the relevant constraints on the size and speed of the turbine and generator are identified in Section 2.6. Third, a simple model for the scaling of the turbine and generator power with rotor speed and device diameter is developed in Section 2.7. Finally, by combining the scaling laws and constraints in Section 2.8, the viable low-flow turbogenerator design space is identified. Within this design space, one specific design is chosen with a 450,000 rpm shaft speed, a 5 mm turbine radius and a 220 um passage height.

Based on the high-level system design developed in Chapter 2, Chapter 3 presents the detailed design and simulation of the turbine designed for low flow and high specific-work operation. First, a 1D mean-line analysis in Section 3.3 determines the required flow angles and pitch-wise averaged mean flow through the turbine. Next, the 2D stage is designed using MISES in Section 3.4, which determines the 2D flow field and profile losses. Finally, in Section 3.5, a RANS 3D CFD simulation with two computational domains, one for the stator and one for the rotor, separated by an interface, is carried out. The simulation validates the

turbine performance of 77 W of shaft power at a mass flow of 1.45 g/s. Note that the 77 W reduces to a 50 W electrical power output after generator and power electronics losses. The focus of the simulation lies on the tip clearance flow and end-wall boundary layers. A second-order formulation and adequate grid density ensure the fidelity of the simulations. A diffuser is used to reduce pressure losses in the right exit turn. The performance of the turbine is assessed in Section 3.5.5, and predicts a total-to-static turbine adiabatic efficiency of 48%. The final high-speed design integrates a MEMS turbine and a meso-scale generator combined with hybrid ball bearings.

4.2.   Conclusions

The research presented in this thesis takes important steps towards the development of a 50 W, low flow turbogenerator design. The design goals of the turbogenerator unit are met in the sense that the device consumes 1.45 g/s and produces 50 W net electric power output. The turbine is successfully designed for a pressure ratio of 5. It is only possible to meet these goals by using a new turbine manufacturing technology, since the required blade span is below the conventional manufacturability limit.

The analysis carried out in Section 2.2 shows that to meet the design goal of reducing mass flow for a given power output, specific work must be maximized, which is equivalent to a high turbine adiabatic efficiency and a high turbine pressure ratio. Section 2.3 shows that the requirement for 50 W operation and reduced flow consumption results in blade spans below the current micro-milling manufacturability limit, thus a new turbine manufacturing technology is required. As discussed in Section 2.5, a single-stage radial inflow turbine design is preferable for low-flow, high specific-work operation. An axial turbine is not feasible due to manufacturing considerations as discussed in Section 2.5.1. A cylindrical-shaped permanent-magnet synchronous generator is preferable for high speed operation as outlined in Section 2.5.2. However, specific design requirements must be met to reduce losses resulting from high speed operation. Generator rotor balancing, mechanical stress and bearing considerations limit the maximum generator speed. Therefore, the integrated turbine and generator design yields a balancing act between blade manufacturability and maximum generator speed. The viable turbogenerator design space illustrated in Section 2.8 is narrowly constrained by the 5-bar

pressure supply and minimum aerodynamically viable blade span. To obviate the design challenge, a high shaft speed near 500,000 rpm is required. However, an increase in speed towards 1,000,000 rpm does not remove the blade manufacturability challenge. To meet the low flow consuption goal and obviate the manufacturing constraint imposed by micro-milling, MEMS DRIE is identified as a required turbine manufacturing technology. The preferred design at 450,000 rpm is thus a silicon etched turbine in combination with a meso-scale custom-made generator. Hybrid ball bearings can operate at rotor speeds of up to 800,000 rpm and are found to be a viable option for high speed operation when simplicity is desired.

It is found that end-wall losses dominate over profile losses, and that turbine performance is very sensitive to tip clearance leakage losses. Thus, the axial displacement of the turbogenerator rotor must be precisely set. Furthermore, the wetted surface in the turbine must be minimized. To reduce the pressure loss in the right exit turns, a diffuser is required. A spacing of 0.3 mm between the rotor and stator must be included to reduce forcing on the stator blades and associated risk of blade fracture.

Overall, this work fits into a trend predicted by [19] which argues that "research at the intersection of macrosystems and power MEMS offers a high innovation potential... through unorthodox combinations of technology." This is exactly what is achieved in this thesis. Here, a MEMS turbine and a meso-scale cylindrical generator are combined to develop a turbogenerator otherwise not feasible with conventional manufacturing approaches. Figure 4-1 illustrates how the effort compares to current design areas and trends. While MEMS designs are scaled up in power, meso-scale devices are scaled down in power. Both trends intersect in the 100 W, 500,000 rpm region.
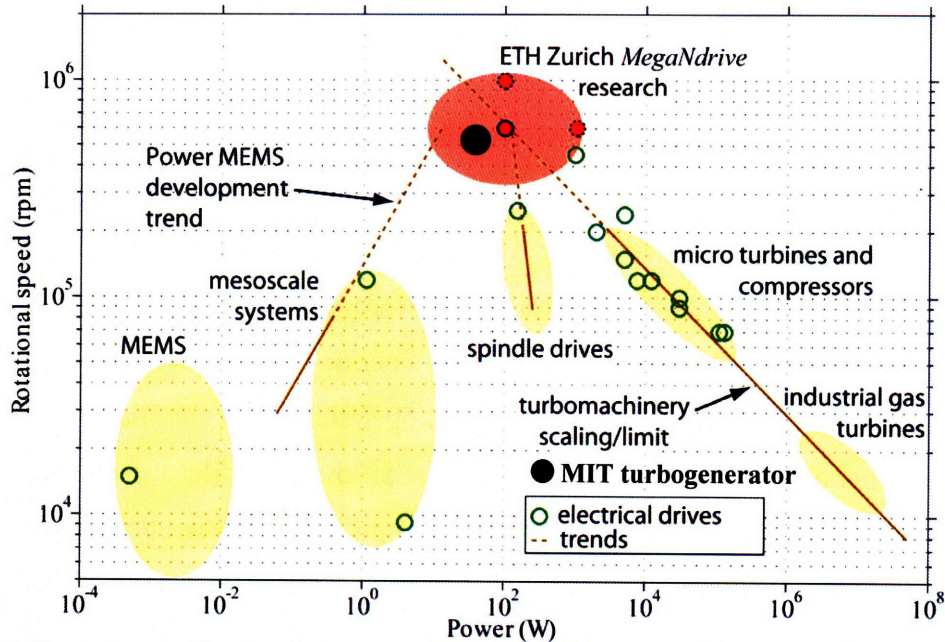
Figure 4-1: Emerging application areas and trends from Power MEMS and turbomachinery [19] and comparison of MIT turbogenerator.

4.3.   Future Work

The immediate next steps towards turbogenerator development should be to fabricate the turbine, possibly design and fabricate a high-speed generator, and assemble and test the device. If the turbine performs as expected and the concept is proven, the next step could be to optimize the system. Since compressed air is considered to be a scarce resource, it is crucial to increase the specific work by increasing the component efficiencies, or by further increasing the operating pressure ratio. As illustrated by

$$PR = [1 - \frac{\gamma - 1}{2} \cdot \frac{\Psi}{\eta^{ad}_T} \cdot M_{U1}^2]^{\frac{\gamma}{(\gamma-1)}}, \tag{4-1}$$

the pressure ratio can be increased by increasing the work coefficient and the tip speed Mach number. Moving to a multi-stage turbine design is another possibility. However, a multi-stage radial turbine design is not feasible because it is judged to be complex and large. A possible solution to this apparent dilemma is an unconventional multi-stage radial design with multiple blade rows on the same disk, similar to the design presented by Deux in [5] or the Ljungstroem steam turbine [7], shown in Figure 4-2. The turbine adiabatic efficiency can be increased by further optimizing the current design, or by using a manufacturing technology that allows the

70

design of 3D diffusers, like e.g. the mold SDM technology [33]. Increasing the turbine pressure ratio from 5 to 8 at constant turbine adiabatic efficiency would further reduce the turbine mass from for 1.45 g/s to 1.2 g/s.

Figure 4-2: Diagram of the Ljungstream steam turbine; the two rows of blades comprising each of the stages rotate in opposite directions so that they can be both regarded as rotors, Figure accepted from [7].

Appendix A.   Numerical Mesh Sensitivity Study

To determine the required grid density for the 3D RANS simulations in Section 3.5, a grid sensitivity study is conducted. Four different grid densities are assumed and Table A-1 summarizes the loss coefficient for the different cases. The coefficient does not change for grids with more than 100,000 cells. The final grid used 225,000 cells.

Table A-1: Variation of stator loss coefficient with stator grid density.

Number of stator cells	50,000	100,000	200,000	500,000
Loss coefficient ω	1.15	1.26	1.27	1.27

Appendix B. Feasibility of Serial Configuration

The challenges outlined in Section 2.3 and the system architecture discussion in Section 2.5 require the analysis of a separate concept where the turbogenerator is placed in series with a load in the one kW range, and where the turbogenerator uses the exhaust air flow from the load. Figure B-1 illustrates the conceptual layout of the alternative turbogenerator configuration. This configuration increases the turbine mass flow and removes the turbine blade manufacturing limitation. The challenge in this configuration is to minimize the load power reduction and to design of a low pressure ratio, high mass flow turbine.
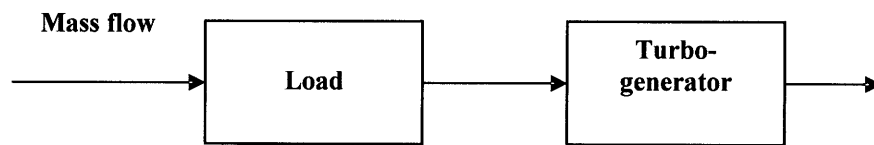

Figure B-1: Schematic overview of alternative turbogenerator configuration.

A high level analysis can be used to determine the reduction in power delivered to the load, to develop a first-pass turbine design, and thus to assess whether the configuration has merit. For this assessment, load powers in the 1 kW to 100 kW range, and 6-bar supply air are assumed. Figure B-2 shows the entropy-enthalpy diagram of the overall configuration. The energy conversion in the load is assumed to be isentropic, and the load exit pressure is used to drive the turbine.
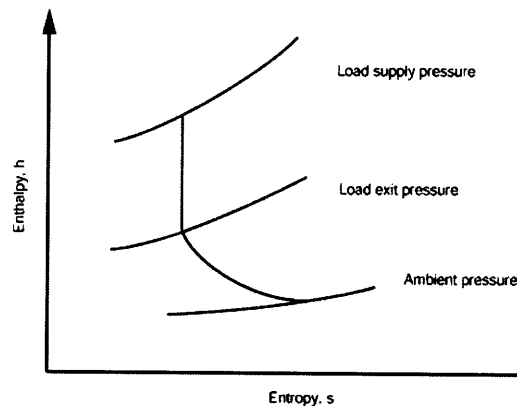

Figure B-2: h-s diagram for serial turbogenerator configuration.

Figure B-3 shows contours of the turbine shaft power for different levels of initial load power and power reduction of the load.
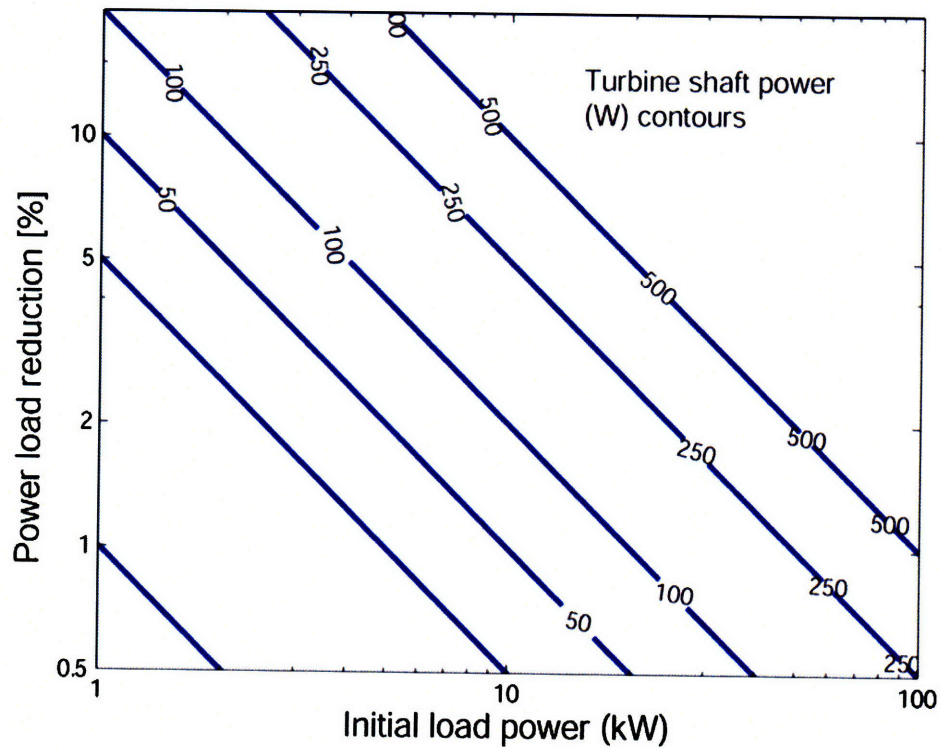

Figure B-3: Contour plot of turbine shaft power for different percentages of work extraction and initial load powers.

Based on the resulting mass flow, the radius of an axial turbine is determined in Figure B-4, assuming a constant hub radius of two millimeters, required by the shaft, and a flow coefficient of 0.6, desirable to minimize the turbine radius.
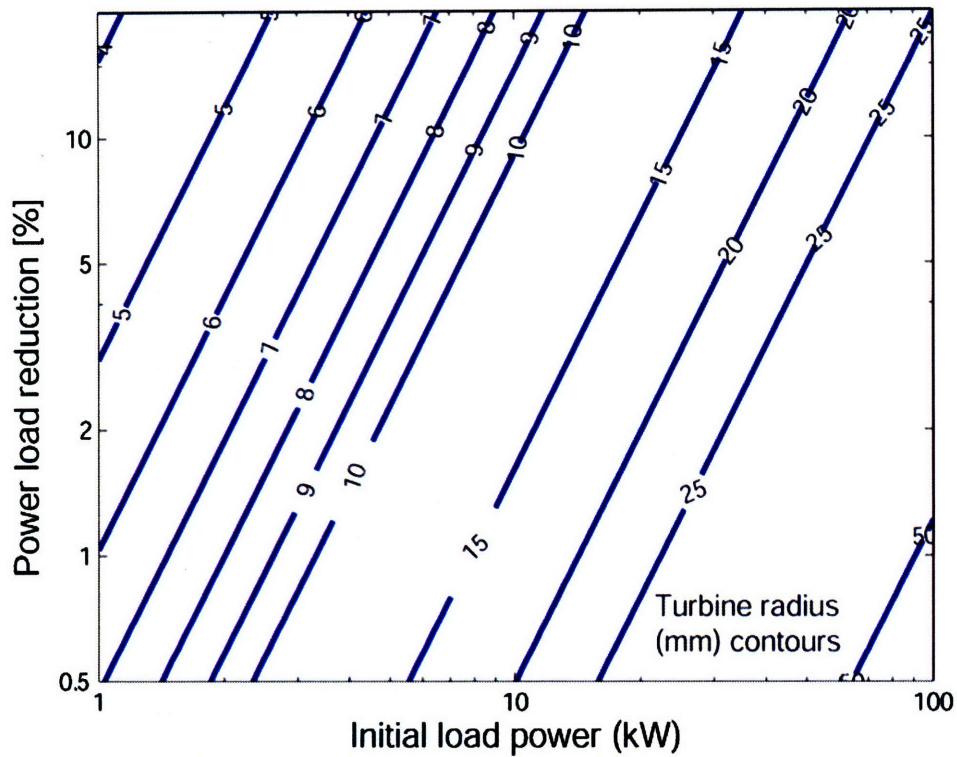
Figure B-4: Contour plot of turbine radius of an axial turbine for different percentages of load work extraction and initial load powers.

In order to minimize the power reduction of the load, it is desirable to operate in the bottom right corner of Figure B-3, and hence the bottom right hand corner of Figure B-4. It is in this corner that 50 W can be extracted from the exhaust of the load without it being a large fraction of the power used by the load itself. However, this yields low turbine pressure ratios, and the turbogenerator design is sensitive to ducting losses. It is concluded that the concept is not feasible due to efficiency considerations, which in return impacts the system architecture, as outlined in Section 2.5.

Appendix C. Low Speed Turbine Design

The design space exploration carried out in Section 2.8 assumed 100 um as the minimum feasible blade span. In order to validate the hypothesis that a planar turbine design with less than 100 um blade spans is not feasible because of low efficiency, a turbine was designed for 150,000 rpm, which is the fastest off-the-shelf generator speed reported in the literature [25]. Table C-1 summarizes the stage performance and all relevant geometric parameters of the low speed turbine design. The relative tip clearance is larger than in the high speed design, thus tip clearance leakage losses are more significant. Furthermore, the blade aspect ratio of 0.1 is lower than in the high-speed design, thus end-wall losses increase.

Table C-1: Summary of low speed turbine stage performance characteristics

P_{shaft}	P_{net}	m	π	Blade span	Tip gap	Rotor radius	Speed
80 W	50 W	4 g/s	5:1	80 um	20 um	12.4 mm	150,000 rpm

Figure C-1 analyzes the performance of the low speed turbine design, illustrating the high exit turn losses, and the high losses in the stator due the small blades. Given the assumptions made (fixed generator speed, high pressure ratio, desired low output power and fabrication constraints) the efficiency is low. The only possibility is to increase the generator speed, which allows for the design of a turbine with longer blade spans, resulting in higher turbine adiabatic efficiency.
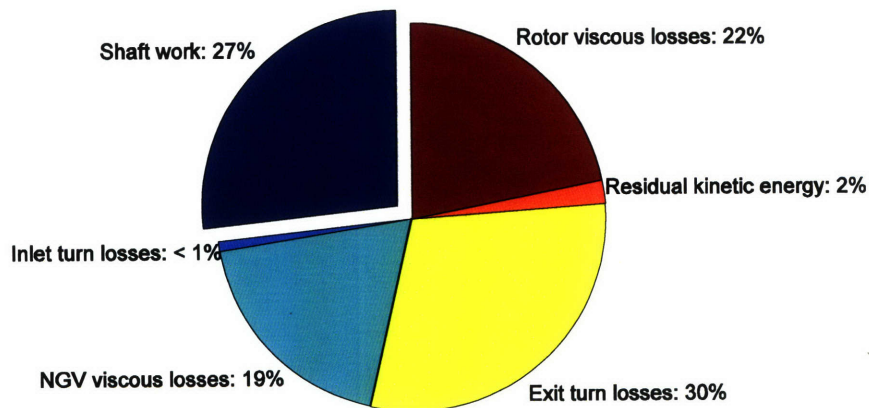

Figure C-1: Loss break-down of low speed turbine design.

Bibliography

[1]   Arnold, D.P., Galle, P., Herrault, F., Das, S., Lang, J.H., and Allen, M.G. A Self-Contained, Flow-Powered Microgenerator System. 2005

[2]   Casey, M.V. The Effects of Reynolds Number on the Efficiency of Centrifugal Compressor Stages. *ASME J. of Eng. for Gas Turbines and Power, Vol. 107, pp. 541-548.* 1985.

[3]   Casey, M.V. Private Communication. 2007

[4]   Das, S. Magnetic Machines and Power Electronics for Power MEMS Applications. Doctoral Thesis, MIT. 2005.

[5]   Deux, P. Design of a Silicon Microfabricated Rocket Engine Turbopump. Master Thesis, MIT. 1998.

[6]   Drela, M., and Youngren, H. A User's Guide to MISES 2.59. 2006.

[7]   Dixon, S. L. Fluid mechanics and thermodynamics of turbo machinery. Elsevier Science & Technology. 2005

[8]   Ehrich, F. F. Handbook of rotordynamics. McGraw-Hill, Ney York, US. 1992.

[9]   Emery, J. C., Herrig, L. J., Erwin, J. R., and Felix, A. R. Systematic two-dimensional cascade test of NACA 65-series compressor blades at low speeds. NACA Report 1368. 1957.

[10]   Fluent Inc. Fluent 5 User's Guide. 2007.

[11]   Greitzer, E. M., Tan, C. S., and Graf, M. B. Internal Flow Concepts and Applications. Cambridge University Press, Cambridge, UK. 2004.

[12]   Haus, H.A., Melcher, J.R., and Cliffs E., N.J. Electromagnetic fields and energy. Prentice Hall. 1989.

[13]   Isomura, K., Tanaka, S., and Kanebako, H. Development of Micromachine Gas Turbines at Tohoku University. *Micro Gas Turbines, pp. 10-1 – 10-34.* 2005.

[14]   Jacobson, S. A. Aerothermal Challenges in the Design of a Microfabricated Gas Turbine Engine. *AIAA-98-2545.* 1998.

[15]   Jacobson, S. A., and Epstein, A.H. An Informal Survey of Power MEMS. *International Symposium on Micro-Mechanical Engineering, December 1-3.* 2003.

[16]   Kafader, U., and Schulze, J. Similarity Relations in Electromagnetic Motors – Limitations and Consequences for the Design of Small DC Motors. *Proc. ACTUATOR 2004, Bremen, Germany, 14 – 16 June, pp. 309 – 312.* 2004.

[17]   Kerrebrock, J. L. Aircraft engines and gas turbines. MIT Press. 1990.

[18]   http://kjmagnetics.com/

[19]   Kolar, J.W., Zwyssig, C., and Round, S.D. Beyond 1,000,000 rpm - Review of Research on Mega-Speed Drive Systems. *Proceedings of the 9th Brazilian Power Electronics Conference (COBEP'07), Blumenau, Brazil, Sept. 30 - Oct. 4.* 2007.

[20]   Kraehenbuehl, D., Zwyssig, C., Weser, H., and Kolar, J.W. Mesoscale Electric Power Generation from Compressed Gas Flow. *Draft.* 2007

[21]   Liu, L.X., Teo, C.J., Epstein, A.H., and Spakovszky Z.S. Hydrostatic Gas Journal Bearings for Micro-Turbomachinery. *J. of Vibration and Acoustics. Vol. 127, pp. 157.* 2005.

[22]   Miller, T.J.E., and Hillsboro, O.H. Switched reluctance motors and their control. Magna Physics Pub. Oxford, Clarendon Press. 1993.

[23]   Moustapha H., Zelesky M.F., Baines N.C. and Japikse D. Axial and radial turbines. Concepts NREC. 2003.

[24]   http://myonic.com/

[25]   Peris, J., Reynaerts, D., and Verplaetsen, F. Development of an Axial Microturbine for a Portable Gas Turbine Generator. *J. Micromech. Microeng. Vol. 13, S190-S195.* 2003.

[26]   Philippon, B. Design of a film cooled MEMS micro turbine. Master Thesis, MIT. 2001.

[27]   Rodgers, C. Small High Pressure Ratio Radial Turbine Technology. VKI Lectures Series 07. 1987

[28]   Rodgers C. and Geiser R. Performance of a high efficiency radial/axial turbine. *Trans. ASME Journal of Turbomachinery 109:151-4.* 1998.

[29]   Rohlik H.E. Analytical determination of radial inflow turbine design geometry for maximum efficiency. NASA TN D-4384. 1978

[30]   Rohlik, H. E. Radial Inflow Turbines. NASA SP-290. 1967.

[31] Srinivasan, K. Integrated design of high-speed permanent-magnet synchronous motor drives. Doctoral Thesis, MIT. 1996.

[32] Teo, C.J. MEMS Turbomachinery Rotordynamics: Modeling, Design and Testing. Doctoral Thesis, MIT. 2006.

[33] Tsuru, H., Sangkyun, K., Johnston, J.P., Toshiyuki, A., Matsunaga, M., and Prinz, F.B. Challenges to Develop Miniature Gas Turbine Engine with Ceramic Unitary Compressor/Turbine Rotor. *International Symposium on Micro-Mechanical Engineering, Vol. 2003(20031130), pp. 296-305.* 2003.

[34] Weser, H. Private Communication. 2007

[35] Whitfield, A. and Baines, N.C. Design of radial turbomachines, Longman, John Wiley and sons, London, UK. 1990

[36] Wilson D.G, and Korakianitis T. The design of high efficiency turbomachinery and gas turbines. Prentice Hall Inc. USA 2nd Edition. 1998

[37] Zwyssig, C., and Kolar, J.W. Design Considerations and Experimental Results of a 100 W, 500,000 rpm Electrical Generator. *J. Micromech. Microeng. Vol. 16, S297-S302.* 2006